

# Plasmonic nanopores for single molecule spectroscopy towards sequencing applications

---

**Paolo Ponzellini**

**12/20/2018**



# Plasmonic nanopores for single molecule spectroscopy towards sequencing applications

---

## Contents

<b>1. Introduction and state of the art</b> .....	5
<b>1.1 Detection methods</b> .....	6
<b>1.2 Biological nanopores</b> .....	6
<b>1.2.1 Biological nanopores applications</b> .....	7
<b>1.3 Solid state nanopores</b> .....	10
<b>1.3.1 Solid state applications</b> .....	12
<b>1.4 Biological-solid state comparison</b> .....	14
<b>1.5 Hybrid nanopores</b> .....	14
<b>1.6 Plasmonic nanopores</b> .....	15
<b>1.7 Conclusions</b> .....	18
<b>References</b> .....	18
<b>2. A Plasmonic zero mode waveguide for single molecule detection through highly confined and enhanced fluorescence emission</b> .....	24
<b>2.1 Introduction</b> .....	24
<b>2.2 Results and discussion</b> .....	25
<b>2.3 Conclusions</b> .....	31
<b>2.4 Methods</b> .....	32
<b>2.4.1 Sample fabrication</b> .....	32
<b>2.4.2 Optical measurements</b> .....	33
<b>2.4.3 Numerical simulations</b> .....	34
<b>2.5 Appendix: Silver-Aluminum nanoslots</b> .....	34
<b>2.5.1 Simulations</b> .....	34
<b>2.5.2 Fabrication</b> .....	35
<b>References</b> .....	36
<b>3. Hollow 3D antennas for site-selective functionalization</b> .....	39
<b>3.1 Introduction</b> .....	39

<b>3.2 Results and discussion</b> .....	41
<b>3.4 Methods</b> .....	49
<b>3.4.1 Optical set-up</b> .....	49
<b>3.4.2 Lifetime measurements</b> .....	50
<b>3.4.3 FRET measurements</b> .....	51
<b>3.4.4 Chemical modification of ATTO dyes</b> .....	51
<b>3.4.5 Electromagnetic Simulations</b> .....	52
<b>References</b> .....	52
<b>4. Controlled deposition of MoS<sub>2</sub> flakes on metallic nanopores by means of an electrophoretic process</b> .....	55
<b>4.1 Introduction</b> .....	55
<b>4.2 Results and Discussion</b> .....	56
<b>4.3 Conclusions</b> .....	62
<b>4.4 Methods</b> .....	63
<b>4.4.1 Exfoliation of MoS<sub>2</sub></b> .....	63
<b>4.4.2 Fabrication of plasmonic nanostructures</b> .....	64
<b>4.4.3 FEM Simulation of MoS<sub>2</sub> flakes integrated over plasmonic nanostructures</b> .....	64
<b>References</b> .....	64

## 1. Introduction and state of the art

The research on single-molecule techniques for biomedical applications, such as DNA sequencing, detection of biomolecules and biological reactions studies, has recently gained considerable momentum.<sup>1-5</sup> In this framework, nanopores, nanometer-scale holes in a thin membrane usually separating two chambers, are emerging as one of the most promising platforms. A key feature of nanopores is that they do not require immobilization of the probed molecules. In a nanopore system, in fact molecules can move to the sensing volume by diffusion or electrophoresis, exploiting the native charge of biomolecules such as nucleic acids, and an applied electric field. Another key feature of nanopores is the ability to linearize or unfold and detect long biopolymer coils through size constriction. When a long biopolymer is threaded through a nanopore only slightly larger than the biopolymer's cross-section, its coil structure is linearized as the polymer passes through the narrow constriction.<sup>6</sup> Such a unique feature is particularly useful for analyzing local structures along a long biopolymer, making nanopores an ideal platform for the development of genomic profiling tools and for DNA sequencing.<sup>7-11</sup>

In 1996 Kasianowicz et al.,<sup>12</sup> by applying an electric field, drove single-stranded RNA and DNA molecules through an alpha hemolysin ( $\alpha$ -HL) embedded within a lipid bilayer membrane. Since the channel diameter could accommodate only a single strand of RNA or DNA, each polymer could cross the membrane as an extended chain, partially blocking the channel. The passage of each molecule could then be detected as a transient decrease of ionic current. The transient decrease duration was proportional to the polymer length and channel blockades could be used to measure the polynucleotide length.

After the milestone paper by Kasianowicz and his collaborators, the field of nanopore sensing has quite developed, thanks to the technological advances in nanotechnology and molecular biology. Several other biological nanopores have been exploited, and solid state nanopores have arisen as an alternative to biological nanopores.

The present introduction gives a short overview over the main features and accomplishments of both biological and solid state nanopores, with a particular attention on the sequencing applications. Solid state hollow nanostructures, namely nanoslots, are considered as well, along with proper nanopores: they don't allow for electrophoretic flow-through experiments, but they can be exploited in diffusion experiments.

Apart from the described DNA and RNA detection, **biological nanopores** have been employed, for example, in detection of nucleotides,<sup>13,14</sup> proteins<sup>15-17</sup> and other small molecules,<sup>18</sup> in the differentiation between different nucleotide conformations,<sup>19</sup> and DNA sequencing.<sup>10,20</sup>

Modern nanofabrication techniques allowed, on the other hand, to fabricate **solid state nanopores** of dimensions of few nanometers, comparable to those of the biological proteins. With respect to biological nanopores, the solid state ones offer the promise of better stability, from the thermal, mechanical and chemical points of view.<sup>21</sup> They have tunable properties such as size, geometry, and surface chemistry in comparison to their biological counterparts.

Hybrid biological-solid state nanopore platforms are under study, as well, with the idea of combining the advantages of both biological and solid-state nanopores.<sup>22,23</sup>

## 1.1 Detection methods

To date, the majority of nanopore sensing studies employed electrical signals for molecule detection and identification. The main technique utilized to achieve sensing by reading electrical signals is resistive pulse sensing, like in the cited experiment by Kasianowicz.<sup>12</sup> The setup for resistive pulse sensing consists usually in two chambers separated by a membrane and filled with an electrolyte. The two chambers communicate via a nanopore and an electrode is placed on both the sides of the membrane. As a constant potential difference is applied between the two electrodes, ions start flowing through the nanopore, and a steady-state ionic current can be measured. The translocation of an analyte from a chamber to the other, determines a partial obstruction of the nanopore channel and hence temporary current modulations. Current modulations can be measured and related to the analyte dimensions, shape superficial charge and interactions with the nanopore.

Electric signal sensing nanopores have proven to be useful in numerous applications, but their further development is hindered by issues such as high-bandwidth electrical noise and low throughput. Then, as described in the next paragraphs, alternative sensing modalities have been explored and are under study, including: tunneling current detection, fluorescence detection, and SERS. In addition, plasmonic techniques are rising as possible tools for improving nanopore based sensing methods.

## 1.2 Biological nanopores

Biological nanopores are found in nature as protein channels that regulate the molecular transport across the cell membrane. They are reproducible with atomic precision and their inner dimensions are compatible with those of many biologically interesting molecules, making them appealing for nanopore sensing. In addition, biological nanopores can be engineered in multiple ways, to adapt the pore to the specific experiment.<sup>24</sup>

The choice of the appropriate biological nanopore for a certain application is based on the geometrical, chemical and stability properties of the nanopores. For example, for molecule translocation experiments, a relevant feature would be the narrowest constriction diameter of the

protein pores in their native forms. Another critical factor is length. The length of the constriction region of the pore strongly affects sensitivity in current measurements. For a strand of DNA, the ion current signal from a given base as it translocates through a nanopore is influenced by neighboring bases, and signal interpretation becomes extremely difficult unless the current signal is more isolated to decrease these contributions from nearby molecules. To give an idea of the dimensions, the distance between two bases is  $\sim 0.34$  nm for ssDNA,<sup>25</sup> and hence about 15 bases will be present at the same time within an  $\alpha$ -HL pore that has a 5 nm long channel. Gating is another issue.  $\alpha$ -HL protein pores remain indefinitely open under a wide range of experimental conditions, providing a stable baseline for molecular sensing experiments. OmpG pores, instead, undergo pH, voltage, and spontaneous gating, because of the mobile loops at the extracellular side entrance.<sup>26</sup> Site-directed mutagenesis has been exploited to minimize OmpG pores gating behaviors, and the obtained “quieter” OmpG pore could be used for ionic resistive pulse sensing experiments.<sup>27</sup>

In terms of native surface properties then, AeL pores are characterized by an inner positive charge, and attract negatively charged analytes. MspA pores and ClyA pores, on the other hand, have negatively charged residues within the pore constriction.

To summarize, each pore has its own features in terms of size, gating behaviors, and surface, that can be exploited for different applications. Sketches of the biological pores listed above are depicted in Table 1.

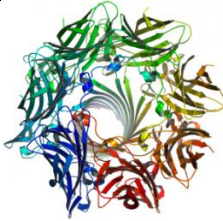
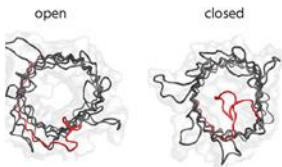
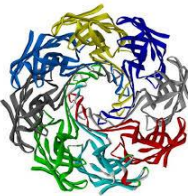
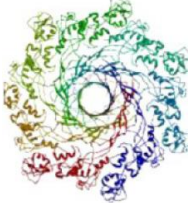

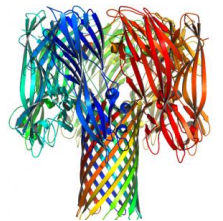
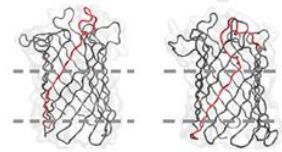

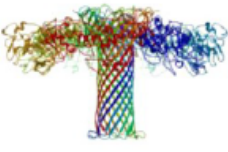

	$\alpha$ -HL <sup>28</sup>	OmpG <sup>27</sup>	MspA <sup>21</sup>	AeL <sup>21</sup>	ClyA <sup>21</sup>
Top view					
Side view					

Table 1. Structure of some of the most commonly used biological pores.

### 1.2.1 Biological nanopores applications.

Following Kasianowicz,<sup>12</sup> several different biological nanopores have been used to detect and identify nucleic acids,<sup>13,14</sup> even in the form of oligonucleotides and mononucleotides,<sup>29</sup> or to distinguish between nucleotide conformations (Fig.1).<sup>19,30</sup>

Direct detection of protein molecules is complicated with biological nanopores, since the diameter of most biological nanopores is smaller than the size of most protein molecules in folded and functional forms.<sup>21</sup> A possible approach makes use of an enzyme motor to induce unfolding of the protein molecules and prompt translocation,<sup>31</sup> while several indirect approaches have been reported.<sup>32,33</sup>

A sensing principle that is unique to biological nanopores is that of the OmpG.<sup>17</sup> In this case the interaction of analyte proteins with OmpG flexible loops leads to a characteristic signal for each protein molecule, in terms of frequency, duration, and open pore current. By analyzing the current patterns, the bound protein molecules can be identified.

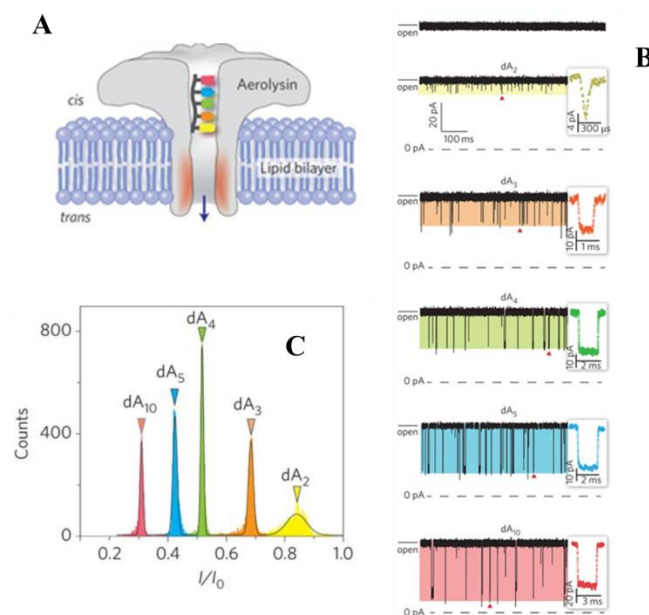


Fig. 1 Applications of biological nanopores for detecting nucleotides. (a–c) Oligonucleotides detection (polydeoxyadenines (dAn),  $n = 2, 3, 4, 5, 10$ ) by means of an aerolysin pore. (a) Short oligonucleotide translocating through a nanopore (aerolysin). (b) From top to bottom, sample current traces for oligonucleotides of different lengths. The blockades marked with the red triangles are magnified in the insets. (c) Blockade events associated with the translocation of the different oligonucleotides, with Gaussian fits. From Cao et al., Nat. Nanotechnol. 2016, 11, 713–718.<sup>19</sup>

Biological nanopores then, have been used in a variety of ways to study different analytes, including nucleic acids, proteins, and even metal nanoparticles, but their most chased application is DNA sequencing. One of the main obstacles in this direction is the fast translocation speed of ssDNA molecules. The most successful approaches to tackle the problem involve DNA polymerase. In 2012, Manrao et al.<sup>10</sup> exploited a phi29 DNA polymerase motor for slowing down the DNA translocation through an engineered MspA nanopore. The phi29 is the same bacteriophage that is itself often employed as the nanopore. In this case, however, its stepwise activity was exploited to



translocate the analyte DNA molecule through the MspA nanopore at 28 ms per base. With such a system, Manrao and coworkers were able to resolve changes in current that correspond to a known DNA sequence. They observed well-resolved and reproducible ionic current levels with median durations of ~28 ms and ionic current differences of up to 40 pA. Using six different DNA sequences with readable regions 42-53 nucleotides long, they recorded current traces that map to the known DNA sequences, achieving single-nucleotide resolution and DNA translocation control. Still, the described system can't achieve direct de novo sequencing: direct translation of the electric signals into reliable sequencing information has not yet been realized, without a reference for alignment. In those studies where the polymerase is not used, DNA generally translocates faster than 1 nucleotide per microsecond, and single nucleotide resolution is not achievable yet. Still in 2012, Fuller et al. first reported the adoption of a nanopore-based sequencing by synthesis (SBS) strategy for DNA sequencing (Fig.2).<sup>20</sup>

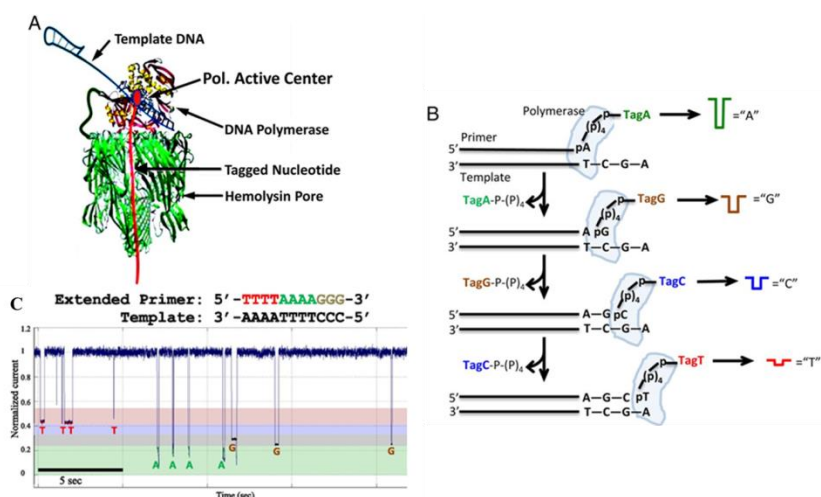


Fig. 2.  $\alpha$ -HL-polymerase for DNA sequencing. (a) Sketch of the sensor design. The  $\alpha$ -HL nanopore is conjugated to a phi29 DNA polymerase molecule. (b) SBS working principle. The tagged nucleotides are sequentially captured and detected while they are attached to the growing DNA strand. (c) Sample homopolymer sequence reads. From Fuller et al. Proc.Natl. Acad. Sci. U. S. A. 2016, 113, 5233–5238.<sup>20</sup>

In SBS, 4 different tags are attached to the 4 different nucleotides. DNA polymerase is exploited here, as well: in nature polymerase synthesizes new copies of DNA through formation of a strand that is complementary to the original template; in SBS, the analyte DNA molecule serves as a template. DNA polymerase adds the complementary, tagged nucleotides that pair with the analyte sequence (e.g.: A→T). During this synthesis reaction, the nucleotide tag is cleaved so that only the native nucleotide is added to the growing strand. The released tag can be identified electrically by the above described resistive pulse sensing method. Again: through the nanopore chosen for the

translocation, a distinct transient current level is observed, associated to a different tag. Despite the outlined achievements, the use of biological pores poses some limitations in DNA sequencing. Apart from the above mentioned stability issues, enzyme motors like DNA polymerase are subject to stochastic skipping and backstepping, and can therefore determine errors in the readout. For practical applications, then, parallel detection would be needed, but mass production of these nanopore-lipid bilayer systems is still challenging, mainly due to the limited stability of the lipid bilayer.

### 1.3 Solid state nanopores

The search for more stable, tunable and scalable sensing systems has stimulated plenty of studies in the field of synthetic nanopores. Synthetic nanopores have been typically fabricated via FIB or TEM milling within synthetic membranes such as silicon nitride ( $\text{SiN}_x$ ) and silica ( $\text{SiO}_2$ ),<sup>34,35</sup> but the fabrication of nanopores has been reported in other materials, including: block copolymers produced by self-assembly,<sup>21</sup> and alumina fabricated through anodic oxidation.<sup>36</sup>

Nanopores have been fabricated in glass, as well, with a simple benchtop method. The tips of electrochemically sharpened Pt microwires have been sealed into glass membranes and then removed, to leave nanopores in their place.<sup>37</sup>

FIB and TEM microscopes allow for milling nanometric pores into silicon and  $\text{SiN}_x$  membranes, directly, at the desired positions and quickly. FIB milling usually can yield nanopores of diameters down to 10÷20 nm, while with TEM one can even obtain subnanometric pores. The nanopores that we have fabricated and that we present in the next chapters, have been realized by means of a gallium FIB. A scanning TEM has been exploited, instead, for example by Rodríguez-Manzo et al., for both thinning a  $\text{SiN}_x$  membrane, by raster scanning the sample, and for drilling holes inside it. Their fabrication led to a 1.4 nm thick membrane with 2.5 nm large holes.<sup>38</sup>

The price for the direct, high resolution of FIB and TEM fabrications is represented by the expensive instrumentation, low sample throughput and scalability, and by the necessity of specialized operators. Dielectric breakdown is an interesting alternative for drilling nanopores inside a dielectric membrane: in 2014, Kwok et al. reported about fabricating holes in dielectric membranes by using tools that are quite more available to researchers, with respect to FIB and TEM microscopes. Their method relies on applying a voltage, through a current amplifier, across an insulating membrane to generate a high electric field, while monitoring the induced leakage current. At voltages up to 20 V across a  $t = 10$  nm or 30 nm thick  $\text{SiN}_x$  membrane, isolated holes start appearing in the membrane, determining observable increases in the recorded current. Single nanopores down to 2 nm in size with sub-nm precision can be fabricated, directly in solution. The nanopores fabricated by this method were shown to produce clear electrical signals from

translocating DNA molecules. Electrical pulses have been used, similarly, to fabricate nanopores within graphene layers.<sup>39</sup>

Dielectric breakdown is a simple and low cost technique but has the disadvantage that the position of the nanopores on the dielectric membrane is random. A solution is provided by plasmonics. As reported by Pud et al.<sup>40</sup>, the dielectric breakdown occurs at lower applied tensions if the electric field is applied in combination with an electromagnetic field shined on the dielectric membrane. Pud and coworkers exploited plasmonic golden bowties to focus the electromagnetic field at the desired position, namely at the center of the bowties. Nanopores are hence formed in correspondence with these plasmonic hotspots. The so called optically controlled dielectric breakdown provides precise control over the nanopore size, so that that these plasmonic nanopores were used by the authors as single molecule DNA electrical sensors with a performance matching that of TEM-drilled nanopores. The fact that the nanopores are automatically fabricated in correspondence with the plasmonic hotspots represents a useful side-effect for plasmonic sensing experiments in translocation: translocating through the nanopore, the analyte is forced to move through the plasmonic hotspot. The concentrated optical field can be used to detect or manipulate the analyte.

A recent tendency in nanopore sensing is represented by ultrathin nanopores. Ultrathin nanopores can be obtained by thinning “regular” dielectric membranes, like in the TEM fabrication described above<sup>38</sup>, or alternatively by drilling holes inside 2D materials like graphene,<sup>41</sup> boron nitride (BN),<sup>42</sup> hafnium oxide(HfO<sub>2</sub>),<sup>43</sup> and molybdenum disulfide (MoS<sub>2</sub>).<sup>44</sup>

2D materials are very attractive for instance for resistive pulse sensing. Their subnanometric thickness is comparable for example with the distance between DNA bases. When a DNA molecule translocates through a 2D nanopore, the ionic current blockade is affected by one DNA base at the time. On the other hand, with thicker nanopores, the current blockade is affected by several DNA bases at the same time, making the signal analysis much more complicated. 2D material should hence offer matchless spatial resolution in this kind of experiments.

A kind of nanopore that, for dimensions and working principle, stands apart from the nanopores mentioned until here are zero mode wave guides (ZMW). ZMWs are nanometric holes, usually fabricated in an aluminum film. Unlike the other nanopores, usually they don't connect two different chambers: they are closed at the bottom. The key design principle of a ZMW is a confined electromagnetic field at the bottom of the nanoholes. Given a certain illumination, the only molecules that feel the light field are the ones located at the bottom of the nanoholes. The rest of the molecules do not feel the light field, due to the screening of the metallic film. As a result, the only fluorophores that can be detected are the ones located in the tiny volume at the bottom of the hole.

A ZMW reduces the detection volume by 3 to 6 orders of magnitude, from  $10^{-15}$  (with a standard confocal microscope) to  $10^{-18}$ – $10^{-21}$  liter, allowing for single-molecule detection at the high ( $\sim\mu\text{M}$ ) analyte concentrations where many biological interesting reactions occur.

ZMWs of different shapes have been designed for single-molecule studies<sup>45–52</sup> and a ZMW is at the base of one of the most successful sequencing device, developed by Pacific Bioscience.<sup>53</sup> The Pacific Bioscience device is a SBS one. DNA polymerase molecules, bound to a DNA template, are attached to the bottom of 50 nm large circular aluminum nanopores (ZMWs). Each polymerase is allowed to carry out second strand DNA synthesis in the presence of fluorescently labeled nucleotides. Each nucleotide is associated to a different dye, and sequencing is performed the same way as in the SBS method described for biological nanopores, except that here the signal is the fluorescence emitted by the different dyes.

### 1.3.1 Solid state applications

In 2001 Li et al. reported the first demonstration of dsDNA detection with a SiNx nanopore by means of the resistive pulse sensing technique<sup>34</sup>. Since then, numerous sensing applications of solid state nanopores have been shown, for different biomolecules. Few representative examples are reported here.

In a famous study of DNA translocation dynamics, Plesa and co-workers translocated linear dsDNA molecules with short oligonucleotide protrusions, acting as markers, attached at determined locations.<sup>54</sup> By monitoring the translocation time of the markers as the DNA was moving through the pore, they measured the translocation speed of different segments along the length of the molecule, observing large intramolecular velocity fluctuations.

Solid state nanopores are used even to discern between different DNA conformations. Carson and coworkers were able to differentiate between the ionic current blockades of deleterious and desired synthesis products.<sup>55</sup> For both nucleic acids and proteins detection, the fast speed of translocation has represented a hurdle for an effective molecule detection. DNA translocation has been slowed down by using the more viscous glutamate (Glu) solutions instead of the conventional  $\text{Cl}^-$  based solutions. For proteins, an example of successful sensing is represented by the detection of bovine serum albumin (BSA) with an  $\text{Al}_2\text{O}_3$  modified nanopore.<sup>56</sup> The  $\text{Al}_2\text{O}_3$  layer, deposited by ALD on the surface, is positively charged at the experimental neutral pH. Therefore, the negatively charged BSA molecule are slightly attracted to the  $\text{Al}_2\text{O}_3$ -coated nanopore walls, and are hence slowed down.

DNA-bound proteins have been detected, as well, as reported by Plesa et al.<sup>57</sup> Here, DNA is translocated through a nanopore in a linear, head-to-tail configuration and the ionic current blockade is measured. The translocation of biomolecules bound to the DNA strand can be detected

as secondary level current changes in addition to the characteristic blockade current for the bare DNA molecules.

For what regards DNA sequencing by electric readout, apart from the usual resistive pulse method, solid state nanopores allow for sensing via tunneling current. Two electrodes are integrated in a nanopore, forming a nanogap. While the analyte translocates through the nanopore, a potential is applied between the two metallic electrodes. The tunneling current between the electrodes at any moment is influenced by the part of the analyte that is inside the pore. It's been calculated that every nucleotide should determine its characteristic current fluctuations.<sup>58</sup> Experimentally, single bases flanked by other bases in a short DNA oligomer have been identified from tunneling current readouts (Fig. 3).<sup>59</sup> Simultaneous detection of DNA molecules with both the tunneling current method and resistive pulse sensing has also been reported.<sup>60</sup>

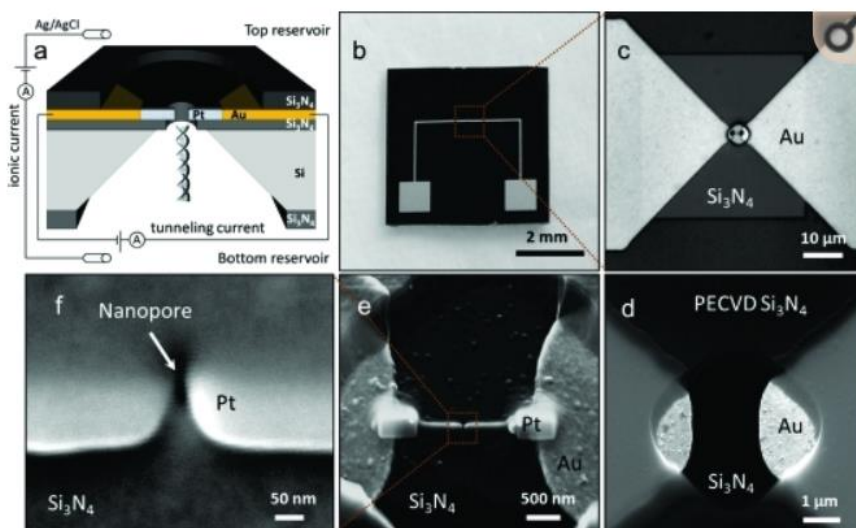


Fig. 3. (a) Sketch of the nanopore/nanogap device. The device is integrated within an electrochemical cell. The tunneling junction is in correspondence with the nanopore. DNA is drawn by means of electrophoresis from the reservoir through nanopore and tunneling junction. (b) The entire chip. Optical image. (c) The golden microelectrodes are aligned with the Free-standing silicon nitride membrane. (d) The window in the silicon nitride membrane, drilled by RIE. SEM image. (e) Top view of the Pt nanoelectrodes. The nanoelectrodes were fabricated by EBID. SEM image. (f) The nanopore is aligned to the Pt nanoelectrodes. SEM image. From Huang S. et al.<sup>59</sup>

All the methods described so far rely on electrical readouts. Fluorescence readout has been exploited for sequencing, as well, but it requires some sample preparation. The distinction among the four types of DNA nucleobases has been achieved by employing biochemical procedures for DNA expansion. Atas et al. converted each nucleobase in each DNA strand into one of four predefined unique 16-mers, preserving the nucleobase sequence.<sup>61</sup>

The resulting converted strands were then hybridized to a library of four molecular beacons, each carrying its specific fluorophore tag, that are perfect complements to the 16-mers used for conversion. Solid-state nanopores were used here to sequentially remove these beacons, one after the other, generating a series of fluorescence signals in four colors that could be optically detected.

A similar approach has been reported, with a different DNA “translation”, into a binary code, with two fluorophores only.<sup>62</sup>

#### **1.4 Biological-solid state comparison**

It is worth summarizing, here, pros and cons of biological and solid state nanopores, with respect to their stability, fabrication scalability, reproducibility, tunability, and surface modifiability.

Compared to their solid state counterparts, biological nanopore systems suffer of a lack of stability, due to the fragility of the lipid membrane that sustains the nanopores themselves. And it is the same fragile lipid membrane that limits the fabrication scalability. On the other hand, solid state membranes (silicon, SiN<sub>x</sub>, glass, polymers...) guarantee much better stability, and solid state fabrication techniques are generally more scalable than the biological ones. From the reproducibility point of view, biological nanopores can be identical the one to the other, atom by atom, and hence are completely reproducible. The other side of the medal, though, is that their design is not very tunable: alterations in biological pore sizes have been developed but require intensive engineering efforts.<sup>29</sup>

On the contrary, solid state nanopores can be designed and fabricated within a large range of dimensions and shapes, at the price of an inferior reproducibility.

Biological nanopores are instead suitable to atomically precise surface modifications, unlike the solid state ones. The crystal structures are known with a high resolution, for the most commonly used biological nanopores: functional groups can be placed exactly at the target locations by means of site-directed mutagenesis.<sup>21</sup> In solid state nanopores, surface modifications regard the entire nanopore surface and surface modification processes have been developed, including: electrostatic adsorption of molecules that have a charge opposite to the nanopore wall surface,<sup>63</sup> ALD deposition of silica or alumina,<sup>64</sup> or even lipid bilayer coatings of the nanopore inner walls.

Last but not least, solid state nanopores are naturally more suitable for integration with other fabricated nanostructures, and electronics and optical readout systems, with respect to biological nanopores.

#### **1.5 Hybrid nanopores**

The different features of biological and synthetic nanopores suggest to design hybrid nanopores to exploit the pros of the two approaches. A typical hybrid system is obtained by substituting the fragile lipid bilayer of a biological nanopores system with a dielectric membrane, like SiN<sub>x</sub>. Such a hybrid system combines the stability of a solid state structure with the atomically-precise reproducibility of the biological nanopores. In 2010 the first hybrid nanopore was reported, consisting in  $\alpha$ -HL biological nanopores inserted in a SiN<sub>x</sub> membrane.<sup>23</sup>

## 1.6 Plasmonic nanopores

Two types of plasmonic nanopore configurations can be considered. Plasmonic nanostructures can be fabricated in proximity of a non-plasmonic nanopore, or the nanopore can be directly fabricated to support, itself, localized plasmons. In both cases the electromagnetic hot-spot generated by the metallic nanostructures can be exploited in several ways for sensing molecules, even at the single molecule level. Examples of plasmonic nanostructures fabricated in proximity of a nanopore include for example golden nanoparticles on a graphene drilled layer<sup>65</sup> and bullseye patterns milled by FIB in a golden layer.<sup>66,67</sup> The plasmonic golden bowties we have mentioned above<sup>40</sup> (facilitating the dielectric breakdown) are a further example. Within that same research group, Nicoli et al. have fabricated the same nanopores configuration, with gold bowtie nanoantennas and a solid-state nanopore at the correspondent plasmonic hot spots.<sup>68</sup> They have applied an electrical tension between the two sides of the membrane and performed DNA translocation experiments and ionic current resistive pulse sensing. By varying the power of the laser that illuminates the nanostructures, they were able to characterize the effects of the plasmonic hotspot on the electric signal. The authors discovered that the Plasmonic excitation of the nanopore influenced both the sensor signal (nanopore ionic conductance blockade during DNA translocation) and the process of the capture of DNA into the nanopore, without affecting the duration of the translocations. Even more interesting, the authors measured a strong plasmon-induced enhancement of the rate of DNA translocation events in lithium chloride (LiCl, already 10-fold enhancement at a few mW of laser power). This provides a means to utilize the excellent spatiotemporal resolution of DNA sensing with nanopores in LiCl buffers, which is known to suffer from low event rates. The authors propose a mechanism based on plasmon-induced local heating and thermophoresis as explanation for the described features. Moreover, the same bow-tie structures fabricated around nanopores have been proposed for rapid DNA sequencing utilizing surface-enhanced Raman scattering from nucleotides passing through the pore.<sup>69,70</sup> Simulations suggest the feasibility of such an approach. Experimental verification is still to come for biological molecules and DNA in particular. To practically realize this platform, precise control over analyte–nanopore interactions will be needed, to obtain accurate Raman signals.



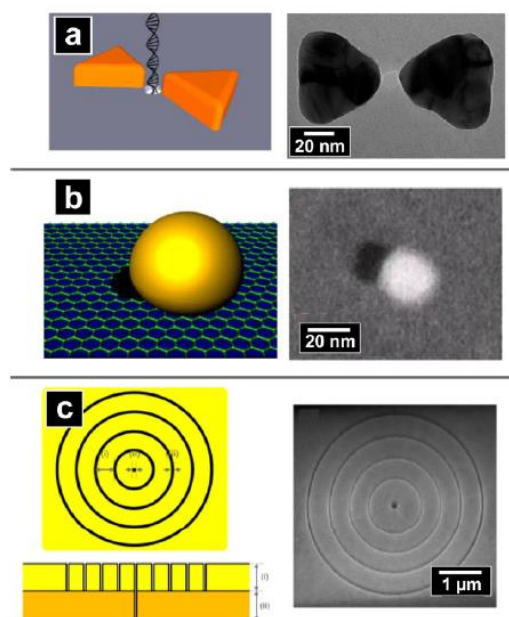


Fig. 4 Examples of different plasmonic nanopore systems. (a) Golden bowtie antenna combined with a 10 nm pore, for DNA translocation. (Left) sketch. (Right): TEM image. From Nicoli, F. et al., *Nano Lett.* 2014, 14, 6917–6925.<sup>68</sup> (b) Graphene nanopore in correspondence with a nanoparticle acting as an optical antenna. (Left): sketch. (Right): SEM image. From Nam, S et al., *Nano Lett.* 2014, 14, 5584–5589.<sup>65</sup> (c) Bullseye plasmonic nanopore. (Left): Sketches of the top view and of the cross-section. (Right): Top-down view of the bullseye structure milled into the membrane. From Crick, C. R. et al., *Nano Lett.* 2015, 15, 553–559.<sup>67</sup>

Plasmonics can even be particularly useful in the fluorescence detection method. In the “Solid state nanopores” paragraph, we have described ZMWs as a tool for shrinking the fluorescence detection volume, in order to diminish the signal noise. Plasmonic optical nanoslots have been fabricated, mainly in silver and gold and in several different shapes.<sup>71–76</sup> They offer the advantage of enhancing the excitation light field at their hotspot and hence the fluorescence signal from the analyte molecules, at the price of a larger detection volume, with respect to proper, non plasmonic ZMWs. As an example, in 2017 Assad et al. have fabricated a dielectric, SiN<sub>x</sub> nanopore at the bottom of a plasmonic golden subwavelength nanoslot, to detect translocating dye-labeled DNA molecules by simultaneously reading an electrical and an optical signal (Fig. 5).<sup>77</sup> The electrical signal was the usual ionic current blockade determined by the pore obstruction caused by the DNA translocation. The optical signal came, instead from the fluorescent dyes attached to the DNA molecule at specific positions.



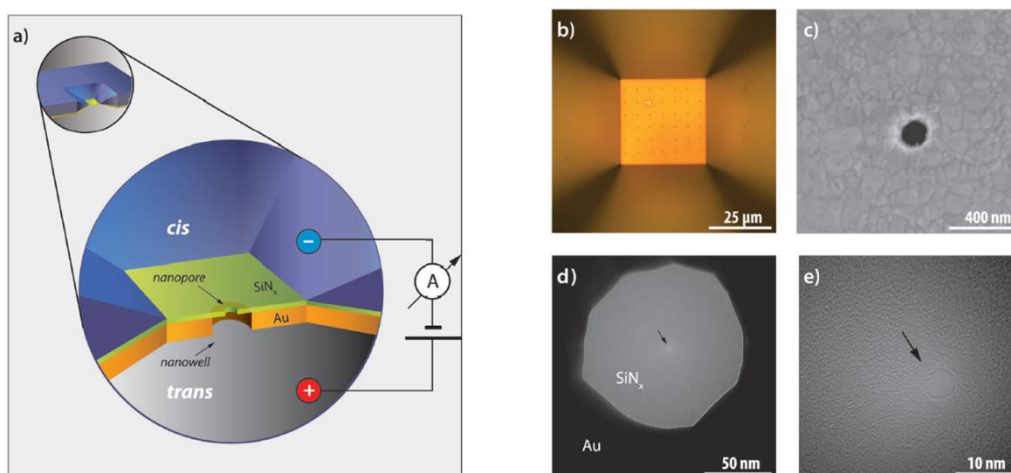


Fig. 5. A plasmonic nanowell–nanopore system for enhanced fluorescence detection at the single molecule level. a) Sketch of the cross-section. The device is constituted by a gold nanowell (orange) and by a nanopore milled inside the freestanding silicon nitride membrane (light green). b) Nanowell array in the free-standing membrane (back side). Optical image. c) Top view of a nanowell. SEM image. d) A nanowell with a nanopore drilled in its base. The nanopore is indicated by an arrow. TEM image. (e) Highly magnified image of the 4 nm pore. TEM image. From O. N. Assad et al, *Adv. Mater.*, 2017, 29, 1605442.<sup>77</sup>

The combined nanopore-nanowell system allowed for sensibly increasing the fluorescence signal to noise ratio. The noise was suppressed thanks to the cladding action of the gold layer and to the gating role of the nanopore: only one molecule (the translocating one) at the time is let into the detection volume in such a system. The plasmonic golden nanoslot instead, provided the field enhancement, and hence the fluorescence enhancement. As mentioned, a second type of plasmonic nanopores can be considered: nanopores can be fabricated, in fact in such a way to resonate, themselves with some incoming laser light, to take advantage from the electromagnetic hotspot generated inside and/or in proximity of the same nanopores. Such plasmonic nanopores are usually prepared in a metal film on a supporting membrane made of a dielectric material, almost always  $\text{SiN}_x$ . As an exception, plasmonic nanopores in a suspended 20 nm gold film has been reported.<sup>78</sup> Sensing by means of this kind of plasmonic nanopores relies usually on the refractometric detection with the same detection principle as in the conventional surface plasmon resonance (SPR) technique.<sup>79</sup> The plasmonic resonant frequency of a nanopore depends on the effective refractive index of the surrounding medium. The refractive index, in its turn, is locally modified by the molecules that are attached to the nanopore walls, leading to a red-shift in the plasmonic resonance.<sup>80</sup> The main difference in methodology for plasmonic nanopores in comparison with SPR is that one can simply measure the transmission spectrum, which can be achieved using a conventional spectrophotometer. Detection through SPR requires slightly more complicated setups. Furthermore, with respect to other plasmonic sensors, the flow-through design of nanopore systems, under certain conditions can increase the rate of binding of the analytes and improve the detection

limit.<sup>80</sup> Another advantage of plasmonic nanopore systems is that their metallic surfaces can be used as electrodes for electrochemistry experiments,<sup>22</sup> for inducing electrophoresis or for applying resistive heating to the system under study. Unfortunately, despite their capability of sensing molecules at very low concentrations, refractometric detection is nowadays inapplicable for real-world uses, because of nonspecific binding in real media, like blood serum. Surface functionalization should be improved in order to reach nonacademic applications.<sup>81</sup> However, refractometric surface sensors can still be useful to study molecular interactions in the absence of interfering species, for instance to deduce binding rates and equilibrium constants.<sup>82</sup>

Beside the refractometric technique, periodic arrays of nanopores in ultrathin Au films were used as substrates for SERS spectroscopy in the optical range, enhancing the signal from oxazine 720 molecules.<sup>83</sup> An additional approach that exploits metallic nanopores is represented by plasmonic optical traps. Within certain nanopore designs (e.g.: a double hole) the trapping event itself appears to generate a clearly detectable intensity change. It is the so called Self Induced Back Action<sup>84</sup> (SIBA). Plasmonic trapping and SERS have been even exploited in combination, for the detection and identification of 20 nm polystyrene nanoparticles in a plasmonic gold nanopore-cavity system.<sup>85</sup>

## 1.7 Conclusions

In the long-term, expansion of the nanopore sensing methods beyond traditional ionic resistive pulse method will continue to push the development of this field. Plasmonic structures can play an important role for solving the current issues and to provide tools for suiting the nanopore sensing techniques to the different applications.

In the next chapters, we describe three different nanopore fabrications that represent little steps in the direction of improving the state of the art single molecule sensing techniques.

In chapter 2 we present a sort of an evolution of a ZMW, capable of combining the features of plasmonic optical nanoslots with the features of traditional ZMWs.

In chapter 3 we move to a flow-through configuration and present a robust protocol for achieving a site-selective fluorophore functionalization for plasmonic nanopores.

Finally, in chapter 4 we introduce a hybrid nanostructure, where MoS<sub>2</sub> flakes are integrated on top of a 3D hollow plasmonic antenna, to combine the advantages of plasmonic and 2D nanostructures.

## References

- 1 J. Shendure, R. D. Mitra, C. Varma and G. M. Church, *Nat. Rev. Genet.*, 2004.
- 2 T. D. Harris, P. R. Buzby, H. Babcock, E. Beer, J. Bowers, I. Braslavsky, M. Causey, J. Colonell, J. DiMeo, J. W. Efcavitch, E. Giladi, J. Gill, J. Healy, M. Jarosz, D. Lapen, K. Moulton, S. R. Quake, K. Steinmann, E. Thayer, A. Tyurina, R. Ward, H. Weiss and Z. Xie, *Science (80-. )*, , DOI:10.1126/science.1150427.
- 3 P. M. Milos, *Expert Rev. Mol. Diagn.*, 2009.
- 4 B. McNally, A. Singer, Z. Yu, Y. Sun, Z. Weng and A. Meller, *Nano Lett.*, 2010, **10**, 2237–2244.
- 5 D. Branton, D. W. Deamer, A. Marziali, H. Bayley, S. A. Benner, T. Butler, M. Di Ventra, S. Garaj, A. Hibbs, X. Huang, S. B. Jovanovich, P. S. Krstic, S. Lindsay, X. S. Ling, C. H. Mastrangelo, A. Meller, J. S. Oliver, Y. V. Pershin, J. M. Ramsey, R. Riehn, G. V. Soni, V. Tabard-Cossa, M. Wanunu, M. Wiggin and J. A. Schloss, *Nat. Biotechnol.*, 2008.
- 6 M. Wanunu, J. Sutin, B. McNally, A. Chow and A. Meller, *Biophys. J.*, , DOI:10.1529/biophysj.108.140475.
- 7 A. Singer, S. Rapireddy, D. H. Ly and A. Meller, *Nano Lett.*, , DOI:10.1021/nl300372a.
- 8 J. K. Rosenstein, M. Wanunu, C. A. Merchant, M. Drndic and K. L. Shepard, *Nat. Methods*, , DOI:10.1038/nmeth.1932.
- 9 B. M. Venkatesan and R. Bashir, *Nat. Nanotechnol.*, 2011.
- 10 E. A. Manrao, I. M. Derrington, A. H. Laszlo, K. W. Langford, M. K. Hopper, N. Gillgren, M. Pavlenok, M. Niederweis and J. H. Gundlach, *Nat. Biotechnol.*, , DOI:10.1038/nbt.2171.
- 11 G. M. Cherf, K. R. Lieberman, H. Rashid, C. E. Lam, K. Karplus and M. Akeson, *Nat. Biotechnol.*, , DOI:10.1038/nbt.2147.
- 12 J. J. Kasianowicz, E. Brandin, D. Branton and D. W. Deamer, *Proc. Natl. Acad. Sci.*, , DOI:10.1073/pnas.93.24.13770.
- 13 S. Howorka, S. Cheley and H. Bayley, *Nat. Biotechnol.*, 2001, **19**, 636–639.
- 14 T. Z. Butler, M. Pavlenok, I. M. Derrington, M. Niederweis and J. H. Gundlach, *Proc. Natl. Acad. Sci.*, 2008, **105**, 20647–20652.
- 15 Y. Wang, V. Montana, V. Grubišić, R. F. Stout, V. Parpura, L.-Q. Gu and L.-Q. Gu, *ACS Appl. Mater. Interfaces*, 2015, **7**, 184–92.
- 16 A. Han, M. Creus, G. Schürmann, V. Linder, T. R. Ward, N. F. de Rooij and U. Staufer, *Anal. Chem.*, 2008, **80**, 4651–4658.
- 17 M. Fahie, C. Chisholm and M. Chen, *ACS Nano*, 2015, **9**, 1089–98.
- 18 J. Ettetdgui, J. J. Kasianowicz and A. Balijepalli, *J. Am. Chem. Soc.*, , DOI:10.1021/jacs.6b02917.
- 19 C. Cao, Y. L. Ying, Z. L. Hu, D. F. Liao, H. Tian and Y. T. Long, *Nat. Nanotechnol.*, , DOI:10.1038/nnano.2016.66.
- 20 C. W. Fuller, S. Kumar, M. Porel, M. Chien, A. Bibillo, P. B. Stranges, M. Dorwart, C. Tao, Z. Li, W. Guo, S. Shi, D. Korenblum, A. Trans, A. Aguirre, E. Liu, E. T. Harada, J. Pollard, A. Bhat, C. Cech, A. Yang, C. Arnold, M. Palla, J. Hovis, R. Chen, I. Morozova, S. Kalachikov, J. J. Russo, J. J. Kasianowicz, R. Davis, S. Roever, G. M. Church and J. Ju, *Proc. Natl. Acad. Sci.*, , DOI:10.1073/pnas.1601782113.
- 21 W. Shi, A. K. Friedman and L. A. Baker, *Anal. Chem.*, 2017, **89**, 157–188.

- 22 W. Shi, Y. Zeng, L. Zhou, Y. Xiao, T. R. Cummins and L. A. Baker, *Faraday Discuss.*, , DOI:10.1039/c6fd00133e.
- 23 A. R. Hall, A. Scott, D. Rotem, K. K. Mehta, H. Bayley and C. Dekker, *Nat. Nanotechnol.*, , DOI:10.1038/nnano.2010.237.
- 24 M. P. Jonsson, A. B. Dahlin, L. Feuz, S. Petronis and F. Höök, *Anal. Chem.*, , DOI:10.1021/ac902925e.
- 25 A. Guasch, J. Pous, B. Ibarra, F. X. Gomis-Rüth, J. M. Valpuesta, N. Sousa, J. L. Carrascosa and M. Coll, *J. Mol. Biol.*, , DOI:10.1006/jmbi.2001.5278.
- 26 S. Conlan and H. Bayley, *Biochemistry*, 2003, **42**, 9453–9465.
- 27 M. Chen, S. Khalid, M. S. P. Sansom and H. Bayley, *Proc. Natl. Acad. Sci. U. S. A.*, , DOI:10.1073/pnas.0711561105.
- 28 Y. Tanaka, N. Hirano, J. Kaneko, Y. Kamio, M. Yao and I. Tanaka, *Protein Sci.*, 2011, **20**, 448–456.
- 29 M. Ayub, D. Stoddart and H. Bayley, *ACS Nano*, 2015, **9**, 7895–903.
- 30 F. Haque, S. Wang, C. Stites, L. Chen, C. Wang and P. Guo, *Biomaterials*, 2015, **53**, 744–52.
- 31 J. Nivala, D. B. Marks and M. Akeson, *Nat. Biotechnol.*, , DOI:10.1038/nbt.2503.
- 32 B. Cressiot, A. Oukhaled, G. Patriarche, M. Pastoriza-Gallego, J. M. Betton, L. Auvray, M. Muthukumar, L. Bacri and J. Pelta, *ACS Nano*, , DOI:10.1021/nn301672g.
- 33 L. Wang, Y. Han, S. Zhou and X. Guan, *Biosens. Bioelectron.*, , DOI:10.1016/j.bios.2014.06.041.
- 34 J. Li, D. Stein, C. McMullan, D. Branton, M. J. Aziz and J. A. Golovchenko, *Nature*, 2001, **412**, 166–169.
- 35 A. J. Storm, J. H. Chen, X. S. Ling, H. W. Zandbergen and C. Dekker, *Nat. Mater.*, 2003, **2**, 537–540.
- 36 E. Choudhary and V. Szalai, *RSC Adv.*, , DOI:10.1039/c6ra13830f.
- 37 B. Zhang, J. Galusha, P. G. Shiozawa, G. Wang, A. J. Bergren, R. M. Jones, R. J. White, E. N. Ervin, C. C. Cauley and H. S. White, *Anal. Chem.*, 2007, **79**, 4778–4787.
- 38 J. A. Rodríguez-Manzo, M. Puster, A. Nicolăi, V. Meunier and M. Drndić, *ACS Nano*, 2015, **9**, 6555–6564.
- 39 A. T. Kuan, B. Lu, P. Xie, T. Szalay and J. A. Golovchenko, *Appl. Phys. Lett.*, , DOI:10.1063/1.4921620.
- 40 S. Pud, D. Verschueren, N. Vukovic, C. Plesa, M. P. Jonsson and C. Dekker, *Nano Lett.*, 2015, **15**, 7112–7117.
- 41 S. Garaj, W. Hubbard, A. Reina, J. Kong, D. Branton and J. A. Golovchenko, *Nature*, , DOI:10.1038/nature09379.
- 42 S. Liu, B. Lu, Q. Zhao, J. Li, T. Gao, Y. Chen, Y. Zhang, Z. Liu, Z. Fan, F. Yang, L. You and D. Yu, *Adv. Mater.*, , DOI:10.1002/adma.201301336.
- 43 J. Larkin, R. Henley, D. C. Bell, T. Cohen-Karni, J. K. Rosenstein and M. Wanunu, *ACS Nano*, , DOI:10.1021/nn404326f.
- 44 K. Liu, J. Feng, A. Kis and A. Radenovic, *ACS Nano*, , DOI:10.1021/nn406102h.

- 45 J. M. Moran-Mirabal and H. G. Craighead, *Methods*, 2008, **46**, 11–17.
- 46 H. J. Levene, J. Korlach, S. W. Turner, M. Foquet, H. G. Craighead and W. W. Webb, *Science (80-. )*, 2003, **299**, 682–686.
- 47 T. Miyake, T. Tanii, H. Sonobe, R. Akahori, N. Shimamoto, T. Ueno, T. Funatsu and I. Ohdomari, *Anal. Chem.*, 2008, **80**, 6018–6022.
- 48 C. I. Richards, K. Luong, R. Srinivasan, S. W. Turner, D. A. Dougherty, J. Korlach and H. A. Lester, *Nano Lett.*, 2012, **12**, 3690–3694.
- 49 H. Rigneault, J. Capoulade, J. Dintinger, J. Wenger, N. Bonod, E. Popov, T. W. Ebbesen and P. F. Lenne, *Phys. Rev. Lett.*, , DOI:10.1103/PhysRevLett.95.117401.
- 50 J. Wenger, P.-F. Lenne, E. Popov, H. Rigneault, J. Dintinger and T. Ebbesen, *Opt. Express*, 2005, **13**, 7035–7044.
- 51 S. Fore, Y. Yuen, L. Hesselink and T. Huser, *Nano Lett.*, 2007, **7**, 1749–1756.
- 52 M. W. Elting, S. R. Leslie, L. S. Churchman, J. Korlach, C. M. J. McFaul, J. S. Leith, M. J. Levene, A. E. Cohen and J. A. Spudich, *Opt. Express*, 2013, **21**, 1189.
- 53 J. Eid, A. Fehr, J. Gray, K. Luong, J. Lyle, G. Otto, P. Peluso, D. Rank, P. Baybayan, B. Bettman, A. Bibillo, K. Bjornson, B. Chaudhuri, F. Christians, R. Cicero, S. Clark, R. Dalal, A. DeWinter, J. Dixon, M. Foquet, A. Gaertner, P. Hardenbol, C. Heiner, K. Hester, D. Holden, G. Kearns, X. Kong, R. Kuse, Y. Lacroix, S. Lin, P. Lundquist, C. Ma, P. Marks, M. Maxham, D. Murphy, I. Park, T. Pham, M. Phillips, J. Roy, R. Sebra, G. Shen, J. Sorenson, A. Tomaney, K. Travers, M. Trulson, J. Vieceli, J. Wegener, D. Wu, A. Yang, D. Zaccarin, P. Zhao, F. Zhong, J. Korlach and S. Turner, *Science (80-. )*, 2009, **323**, 133–138.
- 54 C. Plesa, N. van Loo, P. Ketterer, H. Dietz and C. Dekker, *Nano Lett.*, 2015, **15**, 732–737.
- 55 S. Carson, S. T. Wick, P. A. Carr, M. Wanunu and C. A. Aguilar, *ACS Nano*, 2015, **9**, 12417–24.
- 56 C. Wang, Q. Fu, X. Wang, D. Kong, Q. Sheng, Y. Wang, Q. Chen and J. Xue, *Anal. Chem.*, 2015, **87**, 8227–8233.
- 57 W. Yang, L. Restrepo-Pérez, M. Bengtson, S. J. Heerema, A. Birnie, J. van der Torre and C. Dekker, *Nano Lett.*, 2018, **18**, 6469–6474.
- 58 M. Wanunu, T. Dadosh, V. Ray, J. Jin, L. McReynolds and M. Drndić, *Nat. Nanotechnol.*, 2010, **5**, 807–814.
- 59 S. Huang, J. He, S. Chang, P. Zhang, F. Liang, S. Li, M. Tuchband, A. Fuhrmann, R. Ros and S. Lindsay, *Nat. Nanotechnol.*, 2010, **5**, 868–73.
- 60 A. P. Ivanov, E. Instuli, C. M. McGilvery, G. Baldwin, D. W. McComb, T. Albrecht and J. B. Edel, *Nano Lett.*, 2011, **11**, 279–285.
- 61 E. Atas, A. Singer and A. Meller, *Electrophoresis*, 2012, **33**, 3437–3447.
- 62 B. McNally, A. Singer, Z. Yu, Y. Sun, Z. Weng and A. Meller, *Nano Lett.*, 2010, **10**, 2237–2244.
- 63 Y. L. Ying, Z. Ding, D. Zhan and Y. T. Long, *Chem. Sci.*, 2017.
- 64 P. Chen, T. Mitsui, D. B. Farmer, J. Golovchenko, R. G. Gordon and D. Branton, *Nano Lett.*, , DOI:10.1021/nl0494001.
- 65 S. Nam, I. Choi, C. Fu, K. Kim, S. Hong, Y. Choi, A. Zettl and L. P. Lee, *Nano Lett.*, 2014, **14**, 5584–5589.

- 66 C. R. Crick, P. Albella, H.-J. Kim, A. P. Ivanov, K.-B. Kim, S. A. Maier and J. B. Edel, *ACS Photonics*, 2017, **4**, 2835–2842.
- 67 C. R. Crick, P. Albella, B. Ng, A. P. Ivanov, T. Roschuk, M. P. Cecchini, F. Bresme, S. A. Maier and J. B. Edel, *Nano Lett.*, , DOI:10.1021/nl504536j.
- 68 Y. Li, F. Nicoli, C. Chen, L. Lagae, G. Groeseneken, T. Stakenborg, H. W. Zandbergen, C. Dekker, P. Van Dorpe and M. P. Jonsson, *Nano Lett.*, , DOI:10.1021/nl504516d.
- 69 F. Nicoli, D. Verschuere, M. Klein, C. Dekker and M. P. Jonsson, *Nano Lett.*, 2014, **14**, 6917–6925.
- 70 M. Belkin, S.-H. Chao, M. P. Jonsson, C. Dekker and A. Aksimentiev, *ACS Nano*, 2015, **9**, 10598–10611.
- 71 T. Sandén, R. Wyss, C. Santschi, G. Hassaïne, C. Deluz, O. J. F. Martin, S. Wennmalm and H. Vogel, *Nano Lett.*, 2012, **12**, 370–375.
- 72 J. T. Choy, B. J. M. Hausmann, T. M. Babinec, I. Bulu and M. Khan, *Nat. Photonics*, 2011, **5**, 738–743.
- 73 J. Wenger, D. Gérard, J. Dintinger, O. Mahboub, N. Bonod, E. Popov, T. W. Ebbesen and H. Rigneault, *Opt. Express*, 2008, **16**, 3008.
- 74 I. Bulu, T. Babinec, B. Hausmann, J. T. Choy and M. Loncar, *Opt. Express*, 2011, **19**, 5268.
- 75 Y. C. Jun, K. C. Y. Huang and M. L. Brongersma, *Nat. Commun.*, , DOI:10.1038/ncomms1286.
- 76 H. Aouani, O. Mahboub, E. Devaux, H. Rigneault, T. W. Ebbesen and J. Wenger, *Nano Lett.*, 2011, **11**, 2400–2406.
- 77 O. N. Assad, T. Gilboa, J. Spitzberg, M. Juhasz, E. Weinhold and A. Meller, *Adv. Mater.*, 2017, **29**, 1605442.
- 78 J. Junesch and T. Sannomiya, *ACS Appl. Mater. Interfaces*, 2014, **6**, 6322–6331.
- 79 J. Homola†, , DOI:10.1021/CR068107D.
- 80 A. B. Dahlin, *Analyst*, 2015.
- 81 A. A. Yanik, M. Huang, O. Kamohara, A. Artar, T. W. Geisbert, J. H. Connor and H. Altug, *Nano Lett.*, , DOI:10.1021/nl103025u.
- 82 R. L. Rich and D. G. Myszka, *J. Mol. Recognit.*, 2011.
- 83 \*,† Alexandre G. Brolo, † Erin Arctander, ‡ Reuven Gordon, § and Brian Leathem and K. L. Kavanagh§, , DOI:10.1021/NL048818W.
- 84 M. L. Juan, R. Gordon, Y. Pang, F. Eftekhari and R. Quidant, *Nat. Phys.*, 2009, **5**, 915–919.
- 85 S. Kerman, C. Chen, Y. Li, W. Van Roy, L. Lagae and P. Van Dorpe, *Nanoscale*, 2015, **7**, 18612.



## 2. A Plasmonic zero mode waveguide for single molecule detection through highly confined and enhanced fluorescence emission

### 2.1 Introduction

As mentioned in the first chapter, ZMWs have been widely exploited in single molecule sensing at micromolar concentrations, thanks to their ability of shrinking the detection volume down to  $10^{-18}$ – $10^{-21}$  liters.

ZMWs of different shapes have been designed for single-molecule studies but in most of the cases the confined field at the bottom of the hole presents no significant enhancement. In contrast, plasmonic optical nanoslots, usually fabricated on Ag or Au films can provide electric field and hence fluorescence enhancement (FE). Searching for a structure that could combine the advantages of a ZMWs with those of an optical nanoslots, Zhao and co-workers designed an alternative solution.<sup>1</sup> Their design consists in a rectangular hollow optical nanoslot on a bilayer of gold and aluminum films. They theoretically showed how the bilayer configuration can replicate the field confinement of an aluminum ZMW but offering a significant light field enhancement. These nanoslots combine the advantages of a ZMW and of a plasmonic slot: they can be considered “plasmonic ZMWs”. On the one hand, they reduce the noise by avoiding to excite the molecules that are not at the bottom of the nanoslot. On the other hand, they enhance the light absorption from the fluorescent molecules in that volume, thanks to the plasmonic hotspot at the bottom of the nanoslot.

Starting from the design from Zhao *et al.*,<sup>1</sup> we have fabricated nanoslots in a gold-aluminum bilayer.<sup>2</sup> We have simulated their response when excited by a plane wave, and from the experimental point of view, we have measured their FE and their detection volume. The fabrication has been challenging. We couldn't obtain vertical walls, in our structures. Instead, the walls of the nanoslots show a flared shape. Theoretically, we have demonstrated how a red-shifts is induced in the spectral behavior of the slot by the fabricated flared shape. Then, we have experimentally characterized the performances of the fabricated plasmonic ZMW by means of fluorescence correlation spectroscopy (FCS). With respect to the confocal volume, the detection volume resulted reduced by a factor  $10^5$ . With this detection volume reduction, it is possible to detect a single molecule within  $\mu\text{M}$  concentrated solutions. This concentrations are typical of many biological phenomena.<sup>3</sup> Still using FCS, we have measured a 25-fold FE, with an illumination wavelength of 676 nm, which was the wavelength for which our ideal structures are theoretically optimized.



The outlined results demonstrate that the proposed design improves the performance of a ZMW for fluorescence spectroscopy at the single molecule level. Furthermore, in the spectral simulations our plasmonic ZMW shows a broadband behavior, which could make it useful for multi-color applications, of whom FRET spectroscopy is an example.<sup>4</sup>

## 2.2 Results and discussion

The experimental verifying of the structure proposed by Zhao et al.<sup>1</sup> (Fig. 1a) began by fabricating the two nanostructures: a classic Al ZMW and a Au–Al nanoslot. The preparation of 40 nm wide nanoslots in a 150 nm thick metal film can be performed using different strategies such as electron beam lithography (followed by lift-off), or direct milling of the nanostructure using a focused ion beam (FIB). The first method was discarded because it presents some difficulties during the lift-off process, due to the high transverse aspect ratio and the small size of the structures.

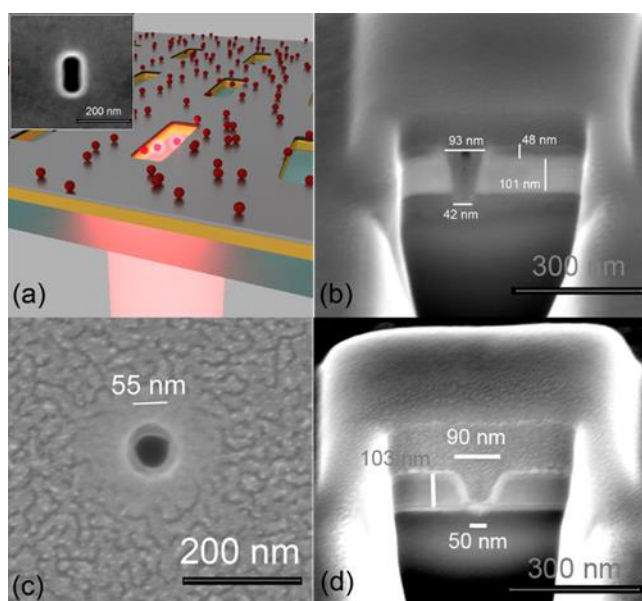


Fig. 1 SEM images of the fabricated structures. (a) Sketch of the Au–Al nanoslots working principle; Inset: top view of a fabricated nanoslot; (b) gold–aluminum nanoslot, cross section. A 101 nm gold layer and a 48 nm aluminum layer are visible. To realize a cleaner and more vertical cross section after the FIB milling, we deposited a platinum layer above the nanostructures: it is the rough material visible in the two cross sections, above the layers and inside the slot. (c) Aluminum ZMW, top view. (d) Aluminum ZMW, cross section. The 103 nm thick aluminum layer is clearly visible, as well as the platinum layer above. From Ponzellini P. et al., *Nanoscale*, 2018, 17362–17369.<sup>2</sup>

The FIB, on the other hand, allows rapid preparation of the nanoslots by direct carving the two-layer film. An inherent disadvantage of FIB milling is the inevitable flared shape of the resulting slots. The two cross sections in Figure 1(b,d) show this phenomenon for the two produced

structures. A second problem of the FIB is the milling depth control. The milling time must be well calibrated to prevent FIB ions from digging inside the glass under the sample. Various cross sections with different milling parameters were used to calibrate the milling time. These cross sections also enabled us to get the correct design parameters for the transverse section. Once we had calibrated the milling parameters, we searched for the best nanoslots and ZMWs in terms of performance. For this purpose, we produced (and measured, like described below) several parametric samples, with gold-aluminum slots and aluminum ZMWs of varying sizes. The reader can find the results of this optimization process in Fig. 4. The fabrication details are given in the Methods section, and the fabricated structures are depicted in Fig. 1(a-inset, c). In light of the plasmonic properties of silver, we have tried to substitute silver to gold, in our fabrications. Unfortunately, the silver-aluminum nanoslots proved to be unstable once in contact with the analyte fluorophore solution, leading to inconsistent measurements. In the appendix more details are given, regarding the fabricated Ag-Al nanoslots.

In Fig. 2 are compared the calculated near fields for our Au-Al nanoslots and for the ideal Au-Al nanoslots as designed in ref. 1. The simulations in ref. 1 concern ideal structures, with vertical walls, while we consider both shapes, with vertical and with inclined walls.

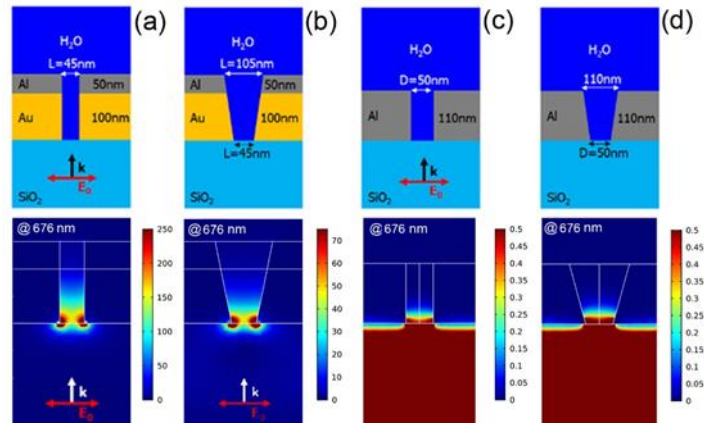


Fig. 2. Sketch of the cross section of: the ideal and actual-fabricated rectangular Au–Al (top panels a–b) and the circular Al (top panel c–d) nanoslot. Near-field intensity distributions of the Au–Al (bottom panels a–b), and Al nanoslots (bottom panels c–d) (ideal and fabricated) at the experimental wavelength. The maximum of the colorbar does not correspond to the field maximum. The section planes of the rectangular slots are parallel to the short axis. From Ponzellini P. et al., *Nanoscale*, 2018, 17362–17369.<sup>2</sup>

This last configuration, as reported above, models the structures made with the FIB. The ideal and the actual-fabricated shapes are shown in the upper panels of Fig. 2 for both the rectangular Au-Al and circular Al ZMWs models.

In the lower panels of Fig. 2(a-d) we represent the distribution of the near field intensity for the ideal and actual gold-aluminum plasmonic ZMWs and aluminum only ZMW. The images are saturated: in each picture, the color bar of the intensity distribution is chosen to make the field distribution more understandable. The field distributions are calculated at 676 nm, as this is the excitation wavelength we used for the experiments, and is even quite close to the resonance wavelength used in the simulations of ref. 1 for the ideal structure (680 nm). For obtaining the near field distributions we used a plane wave excitation, keeping the polarization parallel to the short axis of the structure. We observed that, for both the Au–Al and the Al ZMWs, the e.m. field remains confined at the bottom of the structure. As expected, the Al ZMW does not yield any field enhancement, while the ideal Au–Al nanoslots can give an intensity enhancement of more than 250 at the bottom of the nanoslot. On the other hand, the actual-fabricated structure produced presents a maximum enhancement of the field of a value higher than 75 at the bottom of the nanoslot. These values are related to an increased absorption of light of the fluorescent probe molecule, which diffuses randomly in the nanostructures under consideration. In the appendix it is shown that Ag–Al nanoslots can provide a 120 fold enhancement in the near-field.

In sequencing applications, several dyes are usually needed,<sup>5–7</sup> and these dyes have different excitation and emission wavelengths, the one from the other. The same applies for FRET. In FRET experiments the donor and the acceptor dyes are different in terms of excitation and emission wavelengths.<sup>8</sup> For this reason, it could be very useful to have a plasmonic platform that enhances the fluorescence signal within a wide energy range. Hence, in Fig. 3 we show the computed average near-field intensities vs. the excitation wavelength, for the ideal and actual ZMWs. The computation is performed at the bottom of the ZMWs.

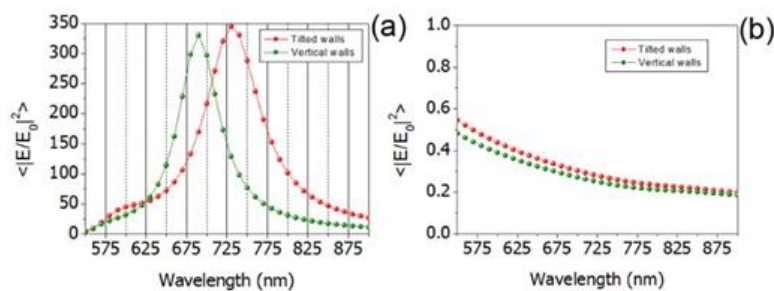


Fig. 3. Calculated field enhancements, averaged on the glass/water interface at the bottom of the two nanostructures. (a) Average field enhancement for the rectangular ideal (green) and fabricated (red) Au–Al nanoslot. (b) Average field enhancement for the rectangular ideal (green) and fabricated (red) Al ZMWs. From Ponzellini P. et al., *Nanoscale*, 2018, 17362–17369.<sup>2</sup>

In the simulations, the nanostructures are excited with a plane wave polarized along the short axis of the structure, with wavelengths in the 550-900 nm range. In the same way as for the simulations

in Fig. 2, we computed here the field enhancement for both the ideal and the actual-fabricated structures. The results in Fig. 3 prove that the flared geometry of the ZMWs we fabricated has to be taken into consideration. The qualitative behavior of the two structures is the same, but the flared shape induces a red-shift in the resonance, with important quantitative effects. In particular, at the experimental excitation wavelength of 676 nm, the average field enhancement is reduced, with respect to the ideal plasmonic ZMWs, from 300 to 100.

For verifying the performances of our plasmonic ZMWs, we have carried out FCS measurements with a solution of Alexa Fluor 680 dyes in water. We illuminated the dyes at 676 nm, because among the wavelengths available to us it was the closest to the spectral maximum of the Au-Al ZMW (see Methods). Since water has a relatively large surface tension, we had to treat each sample with an oxygen plasma, and just after that we could drop the fluorophore solution over the nanoslots. Oxygen renders the metal surface hydrophilic, enabling the fluorophore solution to get into the nanoslots. Details of plasma treatment and optical measurements can be found in the Methods.

Now, by means of the FCS technique, we could characterize each structure by estimating the detection volume reduction (VR), and the FE. We don't report absolute values: VR and FE are normalized to what we can call the confocal experiment, where we measured the detection volume and the fluorescence enhancement values from a drop of Alexa Fluor 680 solution on a cover glass. Confocal measurements were made with two different concentrations (C) of the dyes. For every measurement, we calculated the temporal correlation of the fluorescent signal as  $G(\tau) = \langle F(t)F(t+\tau) \rangle / \langle F(t) \rangle^2$ , where  $F(t)$  is the fluorescence signal,  $\tau$  is the lag time and  $\langle \ \rangle$  indicates time averaging.<sup>9</sup> The data were fitted by means of a Brownian 2D diffusion model (see Methods), to get the average number of molecules  $N$  and the average diffusion time  $\tau_d$ .<sup>9</sup> After that, the count rate per molecule (CRM) was calculated as  $CRM = \langle F \rangle / N$ , and the detection volume as  $DV = N / C$ . The results of the confocal experiments are presented in the following table:

<b>C (nM)</b>	<b>CRM(kHz)</b>	<b>N</b>	<b>DV (p./nM)</b>
0.86	$2.0 \pm 0.9$	2.1	2.41
8.6	$2.3 \pm 0.6$	23	2.67

Table 2: Confocal measurements for different concentrations of Alexa Fluor 680.

CRM is here in thousands of counts per second (kHz) while the DV value is in particles per nM. As we expected, CRM and DV do not depend on the concentration, and we could average out the obtained values to get:

CRM (kHz)	DV (p./nM)
$2.1 \pm 0.5$	$2.54 \pm 0.13$

Table 2: Average results for Alexa Fluor 680 confocal measurements.

For a slot (or ZMW) “i”, VR was calculated as  $VR_i = DV_{\text{conf}}/DV_i$ , while FE as  $FE_i = CRM_i/CRM_{\text{conf}}$ . As previously reported, several Au–Al nanoslots with different sections and volumes were fabricated. By means of FCS, we have determined FE and DV for several samples of every nanoslot. In the following each slot is associated to the FIB software parameters used to fabricate the slots themselves.

Three parameters are given, related to the three different FIB software design dimensions  $(x,y,z)$ .  $x$  and  $y$  correspond to the transverse section of the nanoslot;  $z$  is related to the milling time and therefore to the structure depth. To analyze the performances of the different nanoslots as a function of the design parameter, we calculated the transverse section  $TS = x \cdot y \text{ (nm}^2\text{)}$ , and the volume  $V = x \cdot y \cdot z \text{ (nm}^3\text{)}$  of the nanoslots under study. In Fig. 4 the FEs of some nanoslots are plotted versus TS and versus V. It can be observed how the nanoslot with FIB software design dimensions (60, 130, 30) nm clearly out-performs the rest, therefore we decided to choose it for our fluorescence experiments.

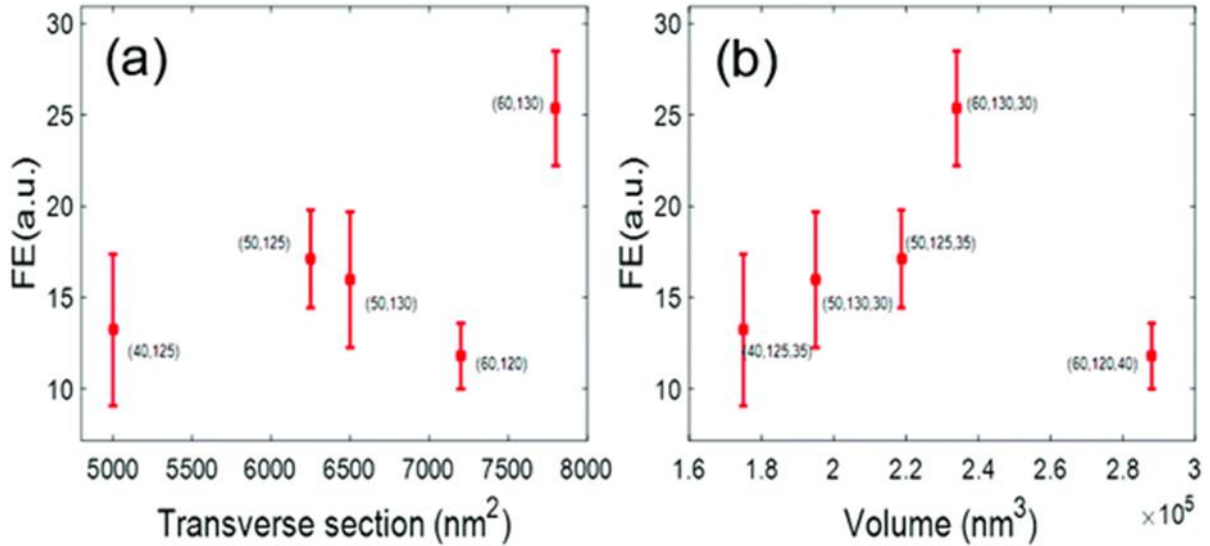


Fig. 4. Fluorescence enhancement measurements with Au–Al nanoslots. (a) Fluorescence enhancement as a function of the theoretical transverse section of the slot. (B) Fluorescence enhancement as a function of the theoretical volume of the slot. All experiments have been done using a concentration of using of Alexa Fluor 680 of 34  $\mu\text{M}$ . From Ponzellini P. et al., *Nanoscale*, 2018, 17362–17369.<sup>2</sup>

According to our cross sections (see Fig. 1(b,d)), choosing 30 nm as the  $z$  FIB parameter should mean milling the metallic bilayer without significantly digging inside the glass substrate; the (60 130) nm  $x$ – $y$  parameters should yield a fabricated transverse section of about  $45 \times 115 \text{ nm}^2$  at the

bottom of the nanoslot. Interestingly, these dimensions are very similar to the ideal simulated  $40 \times 110$  nm dimensions of ref. 1. Regarding the Al ZMWs, we verified an optimum<sup>8</sup> behavior with their parameters set to  $(D,z) = (60,70)$  nm in the FIB software design. Our cross sections (see Fig. 1c), suggest that these parameters should lead to milling through the Al layer and digging inside the glass substrate for a depth of few nanometers. The hole should have a diameter of about 50 nm, at the bottom.

Fig. 5 presents an example of the FCS measurements performed on the optimized structures. In Fig. 5a, we show sample fluorescence signal traces for the Alexa Fluor 680 dye freely diffusing into the Al ZMWs, into the Au–Al nanoslots, and for the confocal configuration.

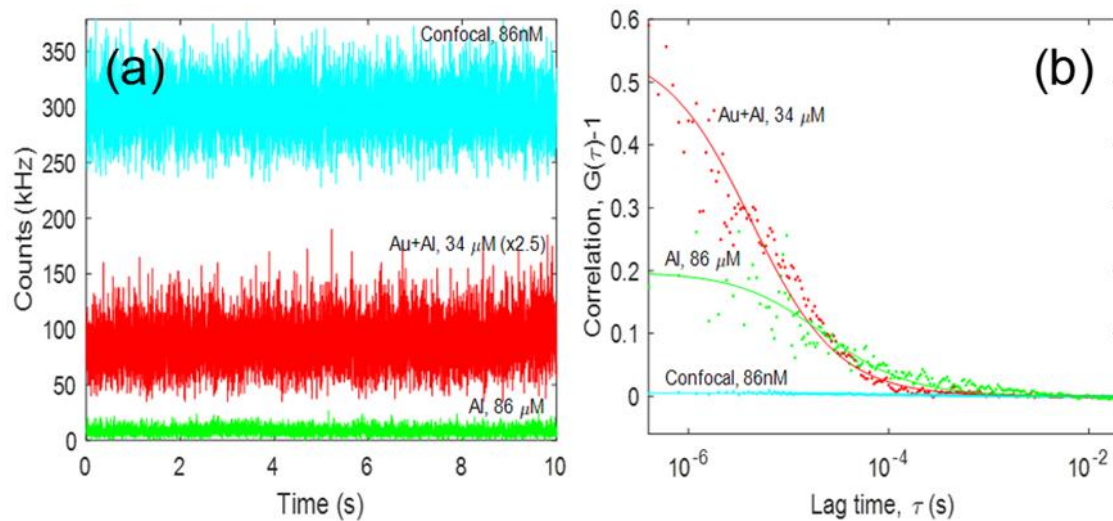


Fig. 5. FCS measurements in Au–Al and Al ZMWs, as well as confocal reference. (a) Fluorescence time traces of representative samples. Note that the Au–Al counts have been multiplied times 2.5 for displaying purposes (b) FCS correlation function (dots, raw data; lines, numerical fits). The cyan traces refer to the confocal reference with a concentration of 86 nM of Alexa Fluor 680; the green traces are obtained with an Al ZMW with a diameter of 60 nm and a depth of 70 nm, using a concentration of 86  $\mu$ M; the red traces are obtained with an optimized Au–Al ZMW at a concentration of 34  $\mu$ M. From Ponzellini P. et al., *Nanoscale*, 2018, 17362–17369.

Fig. 5b shows the autocorrelation function  $G(\tau)$  relative to the three fluorescence signal traces. As intended, the Al and Au–Al ZMWs can work at concentrations of the order of tens of  $\mu$ M and still perform single molecule detection. Table 3 summarizes the performances of the traditional Al ZMWs and of our plasmonic Au–Al nanoslots.

Nanostructure	FE(a.u.)	VR(a.u.)
Al	$1.3 \pm 0.5$	$120000 \pm 10000$
Au+Al	$25 \pm 3$	$110000 \pm 40000$

Table 3: Fluorescence enhancement (FE) and volume reduction (VR) for the optimized slots. The fluorescence enhancement and the volume reduction are calculated with respect to the confocal case.

For the Au–Al ZMW, FE is 25, with respect to the confocal case, while a 5 orders of magnitude reduction is calculated for the detection volume. The diffusion time of the dyes results reduced, as



well, of a factor 20. This is consistent with the values that can be found in the literature.<sup>10</sup> We also note that the FE value for our plasmonic Au–Al nanoslots is 20 times greater with respect to the Al ZMW. At the same time, the detection volumes of the two structures are comparable. These two combined features make the Au–Al ZMWs we fabricated a good candidate for single molecule detection.

Finally, it should be noticed that the near-field intensity calculated for our structures can't be expected to be linearly related to the experimental FE. Firstly, the absorption from the molecule increases when the exciting field increases, and hence increases with FE, but not linearly.<sup>10</sup> There is a saturation threshold in the dyes absorption, over a certain excitation power. The Alexa Fluor 680 dyes is measured to have a CRM of  $2.1 \pm 0.3$  in the confocal experiment: probably the dyes would be already beyond their linear response range, with a 100 fold intensity enhancement. Secondly, the calculated field intensities in Fig. 2 and 3 are not the real field intensities that the fluorophore feels in the experiment: in the experiment we don't excite our structures with a plane wave. We illuminate our structures with a tightly focused Gaussian beam (the microscope objective has a NA = 1.49). Anyway, this wouldn't represent an issue in case of a real application of our structures, since parallel detection typically implies the use of a weakly focused light beam to illuminate a large number of ZMWs at the same time. As a consequence, the calculated high intensities should hold. Third, the fluorescence we measure comes from the dipolar emission of the dyes inside a ZMW. The field enhancement does not determine the Purcell factor, which is the enhancement of the spontaneous emission of dyes. It is the dipole orientation, and the environment around them to determine the Purcell factor.<sup>11</sup> To conclude: the near field simulations are not enough to calculate FE. Additionally, the Alexa Fluor 680 dyes we use have a quantum yield of approximately 0.36, hence it's impossible to increase their emission more than three times. It's easier to get high FE values with low quantum yield dyes.<sup>11</sup> In the end, anyway, there is still a significant correspondence between the near-field intensity simulations in Fig. 2 and 3, and the FE experimental results summarized in Table 3.

## 2.3 Conclusions

In the present chapter we have reported on the fabrication of bilayer plasmonic nanoslots capable of performing enhanced single molecule detection at 10  $\mu\text{M}$  concentrations. The fabrication of the nanoslots by FIB milling has turned out to present some challenges. We did not manage to replicate the original design, that contemplated plasmonic ZMWs with flat walls. Instead, we fabricated nanoslots with a flared shape. We have simulated both the ideal and the fabricated structures and compared their near-field intensity enhancement as well as their spectral properties. The simulations suggest that the Au–Al nanoslots could be used in broadband applications. Finally, we have

experimentally characterized the fabricated structures by evaluating their fluorescence enhancement and the reduction of their detection volume. Compared to the common Al ZMWs, we have measured the same tiny detection volume, but with a 20 folds fluorescence enhancement. In the first chapter we have emphasized how ZMWs are at the base of several reported single molecules sensing experiments and of one of the most successful sequencing devices: these features demonstrate that the fabricated Au–Al nanoslots improve the performance of ZMWs for fluorescence spectroscopy at the single molecule level. And, given that the spectral simulations show that our plasmonic ZMWs have a broadband behavior, we believe that our plasmonic nanoslot could be of great interest for sequencing purposes, where FRET and multiple colors approaches can find an application. Furthermore, the fabricated structure promises to be useful in those fluorescence sensing applications that require a better signal to noise ratio with respect to the traditional Al ZMWs.

A further evolution of the proposed nanostructures could come from drilling a nanopore at the bottom of the nanoslot. It would require a slightly different fabrication: the glass substrate should be substituted by a Si<sub>3</sub>N<sub>4</sub> one and a TEM microscope would be probably necessary to drill a nanopore at the bottom of the nanoslot. With such a fabrication, it would be possible to exploit the advantages of a flow-through configuration, for example by drawing the analytes toward and through the detection volume by means of an electrophoretic force.

## 2.4 Methods

### 2.4.1 Sample fabrication

We used a 150  $\mu\text{m}$  thick glass slide as the substrate. First, we cleaned the substrates thoroughly in order to get a smooth metal surface with the subsequent deposition of the metal. We sonicated the substrates in acetone and isopropanol, then we washed in a piranha solution (3 :: 2 H<sub>2</sub>SO<sub>4</sub> :: H<sub>2</sub>O<sub>2</sub>) and thoroughly rinsed them in deionized and milliq water. We deposited the metal layers by electron beam evaporation in a high vacuum chamber. For all the metal configurations, we used a 3 nm layer of titanium as the linker, to bond the glass substrate to the metal layers. Without this step, delamination of the metal layers would take place, as soon as they came into contact with the fluorophore solution. Such a thin layer of titanium is expected to slightly alter the optical properties of our structures. We evaporate Ti at a 0.3  $\text{\AA s}^{-1}$  rate. For the Al ZMW case, we evaporated a 110 nm Al layer at 1.5  $\text{\AA s}^{-1}$ . For the Au/Al ZMWs we evaporated a 100 nm Au layer at 0.3  $\text{\AA s}^{-1}$  and a 50 nm Al layer at 1.5  $\text{\AA s}^{-1}$ .

For the Ag/al ZMW, we evaporated an Ag 100 nm layer at 1  $\text{\AA s}^{-1}$  and an Al 50 nm layer at 1.5  $\text{\AA s}^{-1}$ .



We milled the nanoslots with a gallium FIB at an accelerating voltage of 30 kV, with a dwell time of 1  $\mu$ s, and with the ionic current set to a low value (7.7 pA) in order to obtain a tiny beam and hence narrow structures. We were not able to clearly distinguish the actual inner geometry of the nanoslots through top view SEM imaging, because of the very high aspect ratio of our nanoslots. Only the upper, outer shape of the structures, at the Al–water interface, was neatly visible and measurable. To evaluate the milling parameters, both the vertical and the horizontal ones, we needed to realize several cross sections on trial nanoslots, on every sample we fabricated (Fig. 1(b,d)). Firstly, this approach allowed us to calibrate the milling time, and hence to reach the glass substrate through the metallic layer, without excessively damaging the glass. Then, it enabled us to measure the slope of the walls of the fabricated nanoslots. With such a calibration we could tune the FIB software design of the nanoslots and obtain the desired rectangular geometry with the optimal simulated dimensions at the nanoslot bottom interface. Those parameters represented a starting point for fabricating parametric samples with nanoslots of various sizes, in a range centered around the dimensions we have simulated. We did the same for the Al ZMWs.

Once prepared, the samples have been kept under nitrogen atmosphere to slow down their deterioration.

Before the FCS measurements, we treated our samples with a 90 seconds oxygen plasma (100% O<sub>2</sub>; 100 W). This was necessary to make their surface hydrophilic enough to let the water solution into the nanoslots.

#### 2.4.2 Optical measurements

For the fluorescence measurements we used an inverted microscope with an oil-immersion 1.49NA microscope objective. The light beam enters the microscope through its rear port and was generated by a continuous ArKr gas laser ( $\lambda = 676$  nm). Before reaching the microscope, the beam was filtered by a bandpass filter 676/29 nm. The power of the laser before entering the rear port of the microscope was 15  $\mu$ W. To handle our samples we used a sample holder attached to a micro and a nanopositioner. Thanks to the nanopositioner we could center the sample with respect to the incoming beam. The nanopositioner was used to move the sample in the  $z$  plane and to reach the height where the fluorescence counts were maximum. We dropped 60  $\mu$ L of Alexa Fluor 680 solution onto the sample and let the dyes diffuse into our structures. We used three filters to separate the fluorescence of the dyes from the reflected light: a dichroic mirror at 685 nm, a longpass filter at 685 nm, and a bandpass filter at 711/25 nm. After the bandpass filter, a 50/50 beam splitter was positioned to split the fluorescence light signal into two different channels. Then to focus the fluorescence signal onto the two equivalent avalanche photodiodes (APD), we used two 50 mm lenses. We recorded the signal coming from the APDs by means of a time-correlated single

photon counting module. We typically recorded 1 minute long fluorescence traces, choosing a 200 ns binning time. After detecting the fluorescence trace, we performed three different calculations to obtain CRM. First, we correlated the fluorescence traces from the two APDs. To fit the autocorrelation function we used a 2D Brownian diffusion model, that allowed us to estimate the average number of molecules,  $\langle N \rangle$ <sup>9</sup>. The 2D model can be used to approximate the 3D diffusion model because the vertical dimension of the detection volume is much greater than its lateral dimensions.<sup>12</sup> Second, we calculated the time average of the fluorescence signal  $\langle F \rangle$  and its standard deviation  $\delta F$ . Third, we calculated CRM as:  $CRM = \langle F \rangle / \langle N \rangle \pm \delta F / \langle N \rangle$ . This was repeated for many nanoslots, to calculate CRM as the average of the CRM values obtained for the measured nanoslots.

### 2.4.3 Numerical simulations

We carried out numerical simulations based on the Finite-Element Method implemented in the RF Module of Comsol Multiphysics® to simulate the electromagnetic behavior of an isolated plasmonic ZMW. We chose the dimensions of the simulated ZMWs according to the sizes measured within SEM observations. We used  $n = 1.33$  as the dielectric constant for water, and  $n = 1.5$  for glass. We used the refractive indexes from Rakic<sup>13</sup> for Au, Ag and Al. The model computes the electromagnetic field in each point of the simulation region, allowing to calculate the quantities plotted in the simulation figures. We set the unit cell to 250 nm in width along both the  $x$ - and  $y$ -directions and to 1000 nm along the  $z$ -direction, with perfect matching layers (150 nm thick) at the borders. A linearly polarized plane wave illuminates the structure from the glass side, the electric field aligned along the short axis of the ZMW.

## 2.5 Appendix: Silver-Aluminum nanoslots

### 2.5.1 Simulations

We have simulated the near field response of the Ag-Al nanoslot at the experimental wavelength of 676 nm (Fig. A1). The simulation has been performed with a plane wave excitation and a polarization parallel to the minor axis of the slot. The results of the simulations resemble those for the Au-Al case, with a strong field enhancement at the bottom of the nanoslot.

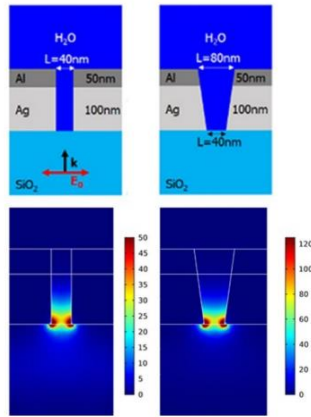


Figure A1. Sketch of a section of the ideal and fabricated rectangular Ag-Al (top panels) nanoslot. In the bottom panels the near field maps for ideal and experimental structures are reported.

The simulated broadband behaviour of the Ag-Al nanoslot is depicted in Fig. A2. Similarly to the Au-Al nanoslot case, the experimental-flared shape induces a red-shift with respect to the ideal shape. Moreover, we observe that the near-field intensity spectra of both the ideal and the experimental shape are blue-shifted with respect to the Au-Al nanoslot. Here the maximum of the average field enhancement is quite higher than that of the Au-Al nanoslot, but it occurs at a wavelength that is far away with respect to our excitation wavelength.

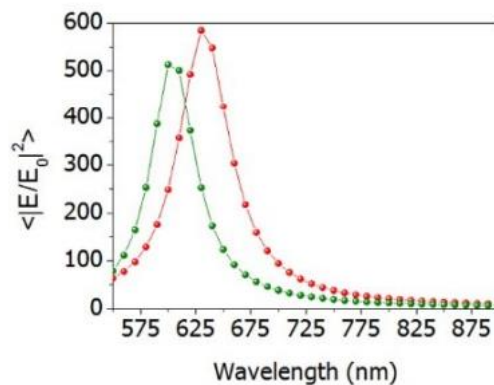


Fig. A2. Calculated field enhancements, averaged on the glass/water interface at the bottom of the Ag-Al nanoslot for the rectangular-ideal (green) and flared-fabricated (red) shapes.

### 2.5.2 Fabrication

Ag-Al samples have been fabricated similarly to the Au-Al ones, the only difference regarding the deposition rates of the different materials (see methods). Here we show a cross section of the milled Ag-Al structures (Fig. A3).

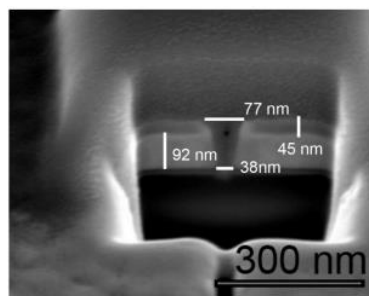


Fig. A3. Silver-aluminum nanoslot, cross section. A 92 nm gold layer and a 45 nm aluminum layer are visible. SEM image.

Once unloaded from the evaporator chamber, these samples have been measured within few hours, to reduce the oxidation. Unfortunately, the Ag-Al samples were unstable when they got in contact with the fluorophore solution. As shown in Fig. A4, they started delaminating after few minutes, thus making it impossible for us to measure their fluorescence response.

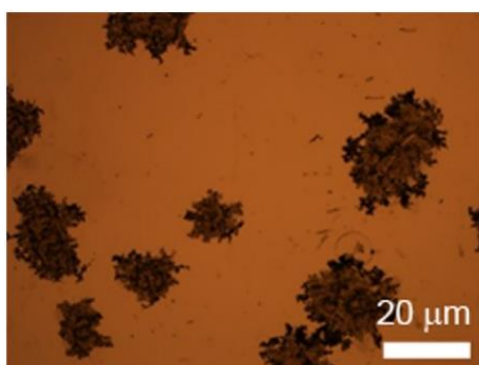


Fig. A4. Delaminated Ag-Al samples. Bright field images.

Alternatively, we thought of doing the fluorescence experiment in ethanol, instead of in water. Ethanol has got a smaller surface tension, with respect to water. Therefore, the ethanol-fluorophore solution can enter the nanoslots without the need of an oxygen plasma treatment. In this way, we could avoid the oxidizing effect deriving from both the contact with water and the plasma treatment. Indeed, the Ag-Al sample were more stable in ethanol, but still we did not manage to gather good data due to the high evaporation rate of ethanol.

## References

- 1 C. Zhao, Y. Liu, J. Yang and J. Zhang, *Nanoscale*, 2014, **6**, 9103–9109.
- 2 P. Ponzellini, X. Zambrana-Puyalto, N. Maccaferri, L. Lanzanò, F. De Angelis and D. Garoli, *Nanoscale*, 2018, 17362–17369.
- 3 D. Punj, P. Ghenuche, S. B. Moparthi, J. de Torres, V. Grigoriev, H. Rigneault and J. Wenger, *Wiley*

*Interdiscip. Rev. Nanobiotechnology*, 2014, **6**, 268–282.

- 4 P. Ghenuche, J. De Torres, S. B. Moparthi and V. Grigoriev, *Nano Lett.*, 2014, **14**, 4707–4714.
- 5 J. Eid, A. Fehr, J. Gray, K. Luong, J. Lyle, G. Otto, P. Peluso, D. Rank, P. Baybayan, B. Bettman, A. Bibillo, K. Bjornson, B. Chaudhuri, F. Christians, R. Cicero, S. Clark, R. Dalal, A. DeWinter, J. Dixon, M. Foquet, A. Gaertner, P. Hardenbol, C. Heiner, K. Hester, D. Holden, G. Kearns, X. Kong, R. Kuse, Y. Lacroix, S. Lin, P. Lundquist, C. Ma, P. Marks, M. Maxham, D. Murphy, I. Park, T. Pham, M. Phillips, J. Roy, R. Sebra, G. Shen, J. Sorenson, A. Tomaney, K. Travers, M. Trulson, J. Vieceli, J. Wegener, D. Wu, A. Yang, D. Zaccarin, P. Zhao, F. Zhong, J. Korch and S. Turner, *Science* (80-. ), 2009, **323**, 133–138.
- 6 D. R. Bentley, S. Balasubramanian, H. P. Swerdlow, G. P. Smith, J. Milton, C. G. Brown, K. P. Hall, D. J. Evers, C. L. Barnes, H. R. Bignell, J. M. Boutell, J. Bryant, R. J. Carter, R. Keira Cheetham, A. J. Cox, D. J. Ellis, M. R. Flatbush, N. A. Gormley, S. J. Humphray, L. J. Irving, M. S. Karbelashvili, S. M. Kirk, H. Li, X. Liu, K. S. Maisinger, L. J. Murray, B. Obradovic, T. Ost, M. L. Parkinson, M. R. Pratt, I. M. J. Rasolonjatovo, M. T. Reed, R. Rigatti, C. Rodighiero, M. T. Ross, A. Sabot, S. V. Sankar, A. Scally, G. P. Schroth, M. E. Smith, V. P. Smith, A. Spiridou, P. E. Torrance, S. S. Tzonev, E. H. Vermaas, K. Walter, X. Wu, L. Zhang, M. D. Alam, C. Anastasi, I. C. Aniebo, D. M. D. Bailey, I. R. Bancarz, S. Banerjee, S. G. Barbour, P. A. Baybayan, V. A. Benoit, K. F. Benson, C. Bevis, P. J. Black, A. Boodhun, J. S. Brennan, J. A. Bridgham, R. C. Brown, A. A. Brown, D. H. Buermann, A. A. Bundu, J. C. Burrows, N. P. Carter, N. Castillo, M. C. E. Catenazzi, S. Chang, R. Neil Cooley, N. R. Crake, O. O. Dada, K. D. Diakoumakos, B. Dominguez-Fernandez, D. J. Earnshaw, U. C. Egbujor, D. W. Elmore, S. S. Etchin, M. R. Ewan, M. Fedurco, L. J. Fraser, K. V. Fuentes Fajardo, W. Scott Furey, D. George, K. J. Gietzen, C. P. Goddard, G. S. Golda, P. A. Granieri, D. E. Green, D. L. Gustafson, N. F. Hansen, K. Harnish, C. D. Haudenschild, N. I. Heyer, M. M. Hims, J. T. Ho, A. M. Horgan, K. Hoschler, S. Hurwitz, D. V. Ivanov, M. Q. Johnson, T. James, T. A. Huw Jones, G. D. Kang, T. H. Kerelska, A. D. Kersey, I. Khrebtukova, A. P. Kindwall, Z. Kingsbury, P. I. Kokko-Gonzales, A. Kumar, M. A. Laurent, C. T. Lawley, S. E. Lee, X. Lee, A. K. Liao, J. A. Loch, M. Lok, S. Luo, R. M. Mammen, J. W. Martin, P. G. McCauley, P. McNitt, P. Mehta, K. W. Moon, J. W. Mullens, T. Newington, Z. Ning, B. Ling Ng, S. M. Novo, M. J. O'Neill, M. A. Osborne, A. Osnowski, O. Ostadan, L. L. Paraschos, L. Pickering, A. C. Pike, A. C. Pike, D. Chris Pinkard, D. P. Pliskin, J. Podhasky, V. J. Quijano, C. Racz, V. H. Rae, S. R. Rawlings, A. Chiva Rodriguez, P. M. Roe, J. Rogers, M. C. Rogert Bacigalupo, N. Romanov, A. Romieu, R. K. Roth, N. J. Rourke, S. T. Ruediger, E. Rusman, R. M. Sanches-Kuiper, M. R. Schenker, J. M. Seoane, R. J. Shaw, M. K. Shiver, S. W. Short, N. L. Sizto, J. P. Sluis, M. A. Smith, J. Ernest Sohna Sohna, E. J. Spence, K. Stevens, N. Sutton, L. Szajkowski, C. L. Tregidgo, G. Turcatti, S. Vandevondele, Y. Verhovskiy, S. M. Virk, S. Wakelin, G. C. Walcott, J. Wang, G. J. Worsley, J. Yan, L. Yau, M. Zuerlein, J. Rogers, J. C. Mullikin, M. E. Hurler, N. J. McCooke, J. S. West, F. L. Oaks, P. L. Lundberg, D. Klenerman, R. Durbin and A. J. Smith, *Nature*, 2008, **456**, 53–59.
- 7 B. McNally, A. Singer, Z. Yu, Y. Sun, Z. Weng and A. Meller, *Nano Lett.*, 2010, **10**, 2237–2244.
- 8 D. W. Piston and G.-J. Kremers, *Trends Biochem. Sci.*, 2007, **32**, 407–414.
- 9 O. Krichevsky and G. Bonnet, *Rep. Prog. Phys.*, 2002, **65**, 251–297.
- 10 D. Punj , R. Regmi , A. Devilez , R. Plauchu , S. B. Moparthi , B. Stout , N. Bonod , H. Rigneault and J. Wenger , *ACS Photonics*, 2015, **2** , 1099 -1107
- 11 X. Zambrana-Puyalto and N. Bonod, *Phys. Rev. B - Condens. Matter Mater. Phys.*, , DOI:10.1103/PhysRevB.91.195422.
- 12 L. Lanzanò, L. Scipioni, M. Di Bona, P. Bianchini, R. Bizzarri, F. Cardarelli, A. Diaspro and G. Vicidomini, *Nat. Commun.*, 2017, **8**, 1–9.
- 13 A. D. Rakić, A. B. Djurišić, J. M. Elazar and M. L. Majewski, *Appl. Opt.*, 1998, **37**, 5271.



### 3. Hollow 3D antennas for site-selective functionalization

#### 3.1 Introduction

In the second chapter we have described a special, plasmonic ZMW of our fabrication. Except from few novel designs we have mentioned,<sup>1,2</sup> ZMWs rely on diffusion, to get the analyte molecules in solution to the sensing volume. Our nanoslots could be provided with nanopores on their bottom, but at the price of a more complicated fabrication, on specific and fragile TEM substrate. This can represent a drawback for example in case of low concentration solutions, where it would require a long time for the analyte to randomly diffuse to the sensing volume. On the contrary, we have described in the first chapter how nanopores offer the possibility to operate in flow-through. Plasmonic nanopores, on their turn, present the further advantage of generating, upon laser illumination, an electromagnetic hotspot. Until now, plasmonic nanopores have been exploited mainly as refractometric sensors, but several recent papers report on plasmonic nanopores where the electromagnetic hotspot is exploited, within optical sensing methods, for reducing the detection volume, localizing the electromagnetic field and increasing the signal-to-noise ratio.<sup>1,3,4</sup> Their strong field gradient then, can allow for slowing down the translocation of an analyte through a nanopore. As a result, plasmonic nanopores find application in single molecule detection and sequencing based on Surface Enhanced Raman Scattering (SERS),<sup>3</sup> as well as in fluorescence spectroscopy experiments,<sup>5,6</sup> like demonstrated in the second chapter. In particular, enhanced fluorescence in plasmonic nanopores has been verified in single molecule DNA detection.<sup>1,2</sup> In these works, one or more nucleotides are tagged with a suitable dye, and their enhanced emission during the nanopore translocation process enables the fingerprint recording of the molecule. It is worth mentioning that fingerprinting of a single molecule has been recently proposed for another important application, i.e. protein sequencing.<sup>7</sup> In a recent article, Van Ginkel *et al.* sequentially read out the signals from a single protein by means of the Förster Resonant Energy Transfer (FRET) between a dye fixed on a nanopore and the dyes attached to the protein.<sup>8</sup> Van Ginkel and co-workers don't use a plasmonic nanopore, but with their proof-of-concept experiment they show the potentiality of FRET to perform single molecule sequencing with a nanopore. Regarding FRET experiments that exploit plasmonic nanostructure, in 2014 Ghenuche *et al.* demonstrated that a plasmonic nanopore can induce a six-fold enhancement in the FRET rate of a single molecule.<sup>9</sup> In addition, in 2016 de Torres *et al.* demonstrated that plasmonic nanoantennas can allow forbidden dipole-dipole Förster energy transfer exchanges.<sup>10</sup> Despite the significant interest growing around this topic, there aren't many works yet about FRET experiments through plasmonic nanopores. Furthermore, no flow-through experiments that exploit FRET for the detection has been reported so far. One of the critical aspects to exploit plasmonics in FRET-based sequencing is to immobilize

one of the FRET pair dyes in proximity of a plasmonic surface. In this regard, surface functionalization procedures for dye attachment have been extensively investigated,<sup>11</sup> but the selective functionalization at the specific positions where the plasmonic structures are placed is still challenging and there are few works only, in literature, on this topic.<sup>12-14</sup> Notice that a proper site-selective functionalization significantly reduces the amount of the background signal coming from the substrate and facilitates the investigation of fluorescent emission from specific isolated points. Fundamental studies in the direction of optimizing the use of plasmonic nanopores are still missing. A first trial fabrication of ours aimed at obtaining a localized functionalization, along with a high field enhancement, is depicted in Fig. 1. It consists in an array of golden plasmonic rings on a dielectric ( $\text{Si}_3\text{N}_4$ ) substrate. With respect to the usual plasmonic nanopores, here the surface of the membrane is not covered in metal: gold is inside the nanopore only. Such a configuration allows to exploit for example thiol groups, that attach selectively to gold, to bind fluorescent molecules of interest to the nanopore only, like showed in the next paragraphs. The fabrication is straightforward: we have sputter deposited 20 nm of gold onto the “back side” of a  $\text{Si}_3\text{N}_4$  membrane, in order to be able to focus the FIB. Then, with various ionic currents we have drilled holes of various dimensions inside the  $\text{Si}_3\text{N}_4$  membrane. To cover the nanopore walls we have sputter deposited gold from the membrane side we had already deposited gold on. In such a way gold enters the nanopore and covers its inner walls. With further sputter deposition we were able to tune the inner diameter of the nanopores down to  $15\div 20$  nm. The ability to tune the pore dimension is of course useful to adapt to different analytes and to generate different field enhancement profiles and intensities.

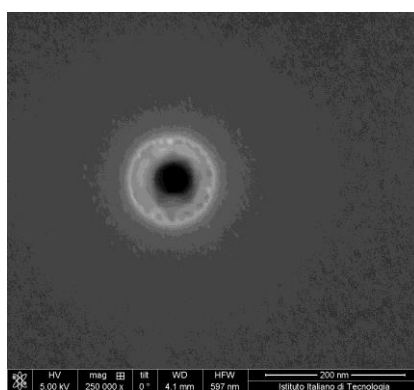


Figure 1. Plasmonic golden nanopore embedded in a dielectric membrane. Front side. Obtained by sputter coating the membrane from the back side.

Unfortunately, it's not straightforward to consistently get rid of the gold deposited on the back side of the membrane only, in order to obtain the golden-nanopore-on-a-dielectric-substrate configuration on both the membrane sides.



While trying to overcome this hurdle, we decided to explore a smarter idea, that involves the 3D hollow antennas whose protocol has been developed in the last years within our group.<sup>15</sup> 3D antennas allowed us to obtain the desired golden-nanopore-on-a-dielectric-substrate configuration with a simple and robust procedure. The substrate was still a Si<sub>3</sub>N<sub>4</sub> membrane (100 nm thick) prepared on a Silicon chip. The fabrication of plasmonic ring nanopore arrays followed the procedure illustrated in Ref.[15] and used by our group in several recent papers . We spun a thin layer of S1813 optical resist on top of the membrane. The resist thickness determines the height of the final structures. Then we drilled holes through the membrane and the resist layer by means of the FIB, from the back side of the membrane. In such a way, around every hole, a hollow cylinder of resist was exposed to secondary electrons generated by the ionic beam. For this experiment, we used four different ionic currents: 80, 230, 430 and 790 pA. With lower currents it would be possible to obtain smaller holes, without compromising the robustness of the fabrication. After the exposure, we developed in acetone and then rinsed in EtOH our samples. The most of the resist layer was melted and removed, leaving only the hollow exposed resist cylinder in their place. Finally, we deposited 3nm of Ti and 30 nm of Au by e-beam evaporation. In order to guarantee much more directionality in the deposition, we chose evaporation, instead of the habitual sputter deposition, and we positioned the sample exactly above the metal crucible, inside the evaporation chamber. In such a way we could avoid the metals to deposit on the side walls of the obtained hollow resist cylinders. We deposited the metal layers at less than 0.3 A/sec, ensuring low roughness. The simple described procedure allowed us to fabricate plasmonic nanopores with a gold ring on top of a dielectric hollow pillar. With such a structure, we were able to site-selectively decorate our metallic nanopores in large arrays with thiol-modified dyes, by means of a single step functionalization method. From the spectroscopic point of view, we used our functionalization method to experimentally characterize the emission efficiency of plasmonic nanopores of four different sizes. As described in the next paragraphs, the characterization was carried out for the single fluorophore and for the donor/acceptor (D/A) FRET configurations.

### 3.2 Results and discussion

Depending on the ionic current used in the milling procedure, the fabricated nanopores were characterized by different hole diameters, spanning from few tens to hundreds of nm. A family of nanopores, with its average diameter, is associated to each of the four milling ionic current. Representative SEM images of illustrative samples are displayed in Fig. 2. We prepared the pillars in 30x30 micron arrays, with a 5 micron distance between adjacent pillars. The average dimensions of the four families of samples are given in Table 1.

Notation	$D_{in}$ (nm)	$D_{out}$ (nm)
A	$70 \pm 30$	$230 \pm 30$
B	$170 \pm 30$	$310 \pm 40$
C	$250 \pm 60$	$370 \pm 10$
D	$330 \pm 40$	$500 \pm 10$

**Table 1.** Notation and average inner ( $D_{in}$ ) and outer ( $D_{out}$ ) diameters of the four different families of fabricated nanopores.

Different diameters are expected to generate different field confinement and enhancement inside different nanoholes. We used Finite Element Methods (FEM) simulations implemented in Comsol Multiphysics with the Radio Frequency Module to investigate the behaviour of the fabricated structures.

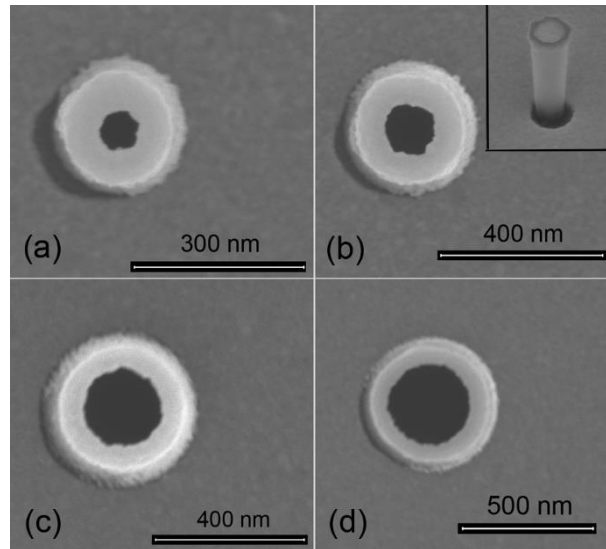
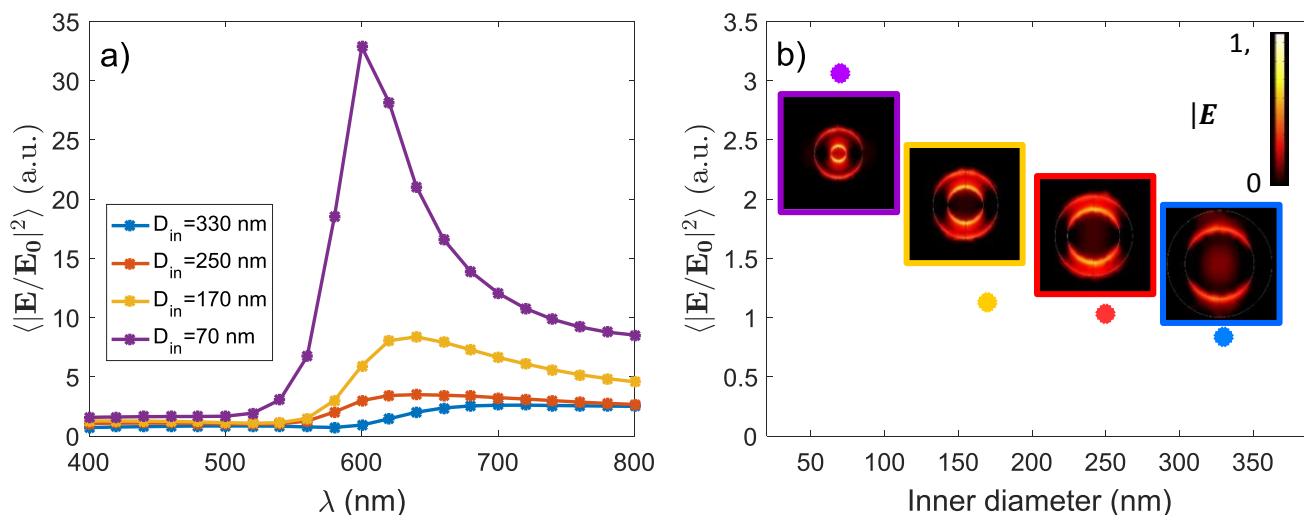


Figure 2. SEM images of the fabricated nanopores. (a) Nanopore fabricated with 80pA ionic current; (b) Nanopore fabricated with 230 pA (inset: tilted view of the dielectric pillar and the metallic ring at the top); (c) Nanopore fabricated with 430 pA; (d) Nanopore fabricated with 790 pA. From Zambrana-Puyalto X. et al., submitted 2018.<sup>16</sup>

Fig. 3(a) presents the spectra of the four average structures. The spectra are calculated under a tightly focused Gaussian beam. It can be observed a red-shift in the spectrum of the nanopores, as the inner diameter increases. Furthermore, the smaller the structure, the higher is the field enhancement in the ring volume. Then, in Fig. 3(b), we calculate the field intensity enhancement

$\langle |E/E_0|^2 \rangle$  averaged on the whole volume of the nanopore (see Methods). The illumination is a tightly Gaussian beam, and the wavelength is 532 nm, like in the experiments (see Methods).



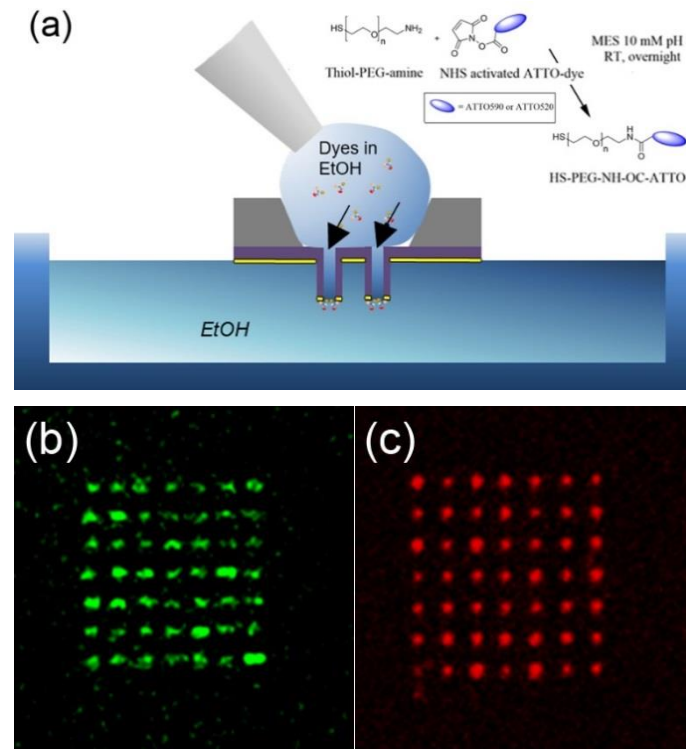
**Figure 3.** (a) Computed spectra of the intensity enhancement for the four nanopores excited with a tightly focused Gaussian beam. (b) Computed field intensity enhancement for the four different fabricated nanopores, averaged out on the volume of the plasmonic nanopores. The simulations were done for a linearly polarized Gaussian beam that is tightly focused ( $w_0 = 350$  nm) at 532 nm. Insets: near-field profiles. From Zambrana-Puyalto X. et al., submitted 2018.<sup>16</sup>

Again, the field enhancement that the dyes feel increases if the size of the nanopore is decreased. Also, the near-field simulations in the insets of Fig. 3(b), show that the enhanced field fills the whole volume of the pore in the smallest nanopore ( $D_{in} = 70$  nm) only. For the bigger nanopores, the field is localized mainly around the nanopore. This agrees with some results reported about similar structures.<sup>17</sup>

The fabricated nanopores (Fig. 2) have the desired structure, with an isolated gold ring on top of a dielectric tube, that allows to perform our functionalization. Furthermore, the hollow structures can be used as nanochannels where molecules can translocate/diffuse through. The functionalization method we present is inspired by a recent functionalization scheme, reported for 2D materials.<sup>18</sup> It is based on the conjugation between gold and a thiolate-dye (Fig. 4). In particular, to obtain a site selective functionalization of our metallic pores, we chose a HS-PEG2000-NH<sub>2</sub> molecule as the linker between the gold covered surfaces and the NHS-activated ATTO dyes. The PEG2000 molecule diameter is about 6 nm, but lower linker lengths could be obtained with shorter PEG molecules.<sup>19</sup> The procedure of functionalization of the dyes is presented in the Methods section. Here we report the protocol for decorating the nanopores<sup>16</sup> (Fig. 4-Top Panel):

- 1) A 50  $\mu$ M solution of HS-PEG-NH-OC-ATTO dye is prepared in EtOH.
- 2) The plasmonic nanopores are prepared on a Si<sub>3</sub>N<sub>4</sub> membrane. The metal is only deposited on the front side of the substrate (see Methods).
- 3) The sample is cleaned in oxygen plasma for 180 seconds to facilitate the diffusion of the dyes through the nanochannels. The surface that is cleaned is the back side, the one with no metal.
- 4) We suspend the sample

on top of an EtOH bath. The metallic face of the sample is in contact with the EtOH bath, whereas the  $\text{Si}_3\text{N}_4$  face is in contact with the air. 5) We wet the dry side with a 3  $\mu\text{L}$  droplet of HS-PEG-NH-OC-ATTO diluted in EtOH. Due to the different concentration, the dyes move towards the EtOH bath and they get attached to the metallic part when they try to reach it. 6) Before the droplet containing the solution with dyes starts to dry off, we add another droplet of 3  $\mu\text{L}$  of the same solution. We repeat this step for three times. 7) The sample is rinsed off in a second pure EtOH bath, and the site-selective functionalization is achieved. It is worth mentioning that we chose EtOH in order to avoid increasing the wettability of the nanopores.



**Figure 4.** (Top-panel) (a) Sketch of the site-selective functionalization process. The front side of the membrane, with the nanopores, is in contact with an EtOH bath. The back side of the membrane is in contact with a solution of dyes in EtOH. The dyes diffuse through the channels and get attached to the nanopore thanks to the thiol group. (Bottom-panels) Fluorescence images of plasmonic nanopores site-selectively decorated with fluorophores. (b) The nanopores are functionalized with ATTO520 dyes. The laser excitation is at 488nm and the fluorescence detection is in the 500-550nm range. (c) The nanopores are functionalized with ATTO590 dyes. The laser excitation is at 561nm and the fluorescence detection in the 570-620nm range.<sup>1</sup> From Zambrana-Puyalto X. et al., submitted 2018.<sup>16</sup>

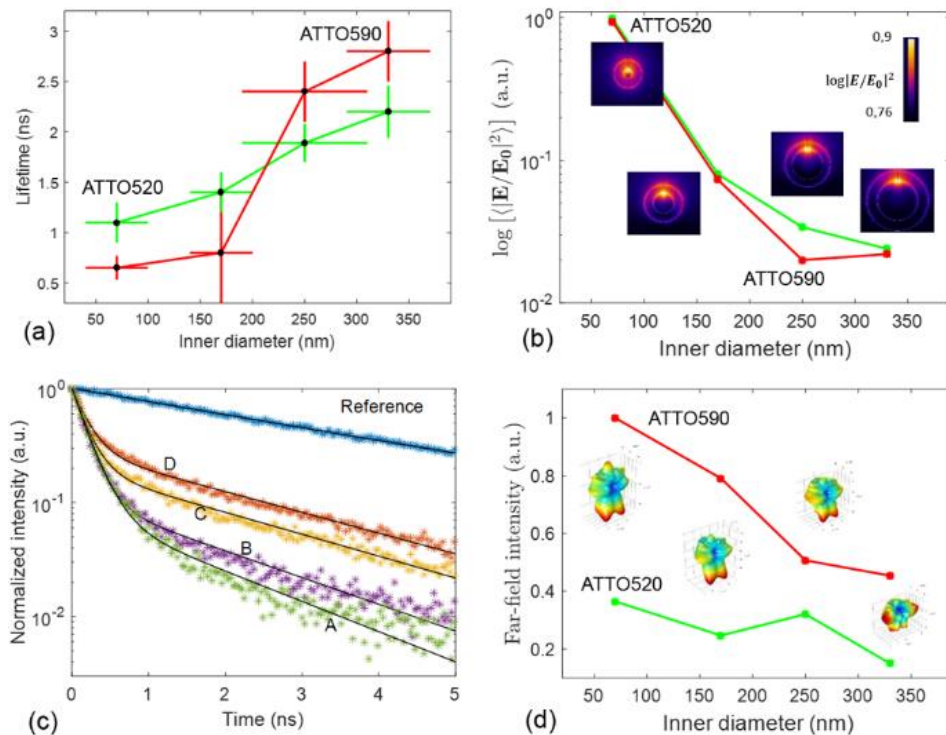
Our configuration, with plasmonic nanopores isolated from the substrate, allows us to get rid of background contributions, but this method of site-selective functionalization could be used even on any nanostructure that contains nanochannels. The thiol-terminated dyes strategy is suitable for noble metals, but the functionalization scheme could be applied also to other materials by exploiting other functional groups.<sup>11</sup> The confocal images in Fig. 4(b,c), taken with a Nikon A1 confocal microscope, show the fluorescence from two different samples functionalized with ATTO520 and

<sup>1</sup> Note that for lifetime measurements we used a different setup.

ATTO590 respectively. As hoped, the fluorescence comes mainly from the nanopore tips, proving a site-selective functionalization. It can be even noticed how the fluorescence intensity varies from pore to pore. The reason is that our protocol does not enable us to attach a predetermined number of molecules to the metallic surface. Anyway this is not an issue for the lifetime studies we present here, since our lifetime experiments do not depend on the number of molecules.

Verified the proper functioning of our site-selective functionalization protocol, we could start investigating the emission behaviours of the ATTO520 and ATTO590 dyes. As mentioned above, we have studied the fluorescence emission of the two dyes in two different configurations: single dye and FRET (D/A) pair. For both the configurations, we have considered the four different families of antennas whose average dimensions are summarized in Table 1.

For the lifetime measurements we used a pulsed laser ( $\lambda=532\text{nm}$ ). We have used two detection channels: one channel to detect the fluorescence from the ATTO 520 dyes in the 553-577 nm spectral band, the other to detect the fluorescence from the ATTO 590 dyes in the 593-643nm spectral band.



**Figure 5.** (a): Lifetime measurements of plasmonic nanopores site-selectively functionalized with single ATTO 520 and ATTO 590. Plotted versus the inner diameter of the nanopore. Each data point is the result of the average of the measurement taken on two arrays of 49 nanopores (see Methods). The fluorescence from the ATTO 520 (590) dyes has been measured in the 553-577 (593-643) nm spectral band. (b): Average calculated intensity emitted by an electric dipole in the nanopore volume. The dipoles emit at 565nm and 618nm respectively. The insets are near-field distributions of the field induced by the dipole emitting at 565nm. (c): Representative lifetime measurements of the four nanopores, as well as the reference case. (d): Far-field intensity emitted by dipoles emitting at 565 nm and 618nm. The far-field is measured on a horizontal plane on top of the nanopore. The insets are the far-field distributions induced by the emitting dipole at 618 nm. From Zambrana-Puyalto X. et al., submitted 2018.<sup>16</sup>

The details about the lifetime measurements of the ATTO dyes emission and about the optical set-up can be found in the Methods section. Figure 5(c) shows a representative measured lifetime trace for each of the four families of structures, decorated with ATTO 520 dyes only. As a reference, we include a lifetime trace measured from a droplet of ATTO 520 dyes thiol-functionalized dropped on the golden flat surface of the same sample. Fig. 5(a) shows the lifetimes measured for the four different fabricated arrays of nanopores, separately functionalized with single ATTO 520 and 590 dyes. To calculate each data point in Fig. 5(a) we averaged out about 100 lifetime measurements (details in the Methods section). Evidently both dyes show the same qualitative lifetime vs nanopore size tendency. The lifetime decreases as the nanopore diameter decreases.

The reason is intuitive: with smaller pores, the emission of the dyes is more likely reflected off the antennas to be absorbed back by the emitting dye itself, and the emission rate results enhanced. On the other hand, to understand why the lifetime reduction is steeper for the ATTO 590 with respect to the ATTO 520, we had to perform some calculations. In these simulations we investigated the emission of an electric dipole emitting at 565nm (representative of the ATTO 520 dye) and at 618nm (ATTO 590). In the simulations the dipole is set at 6 nm off the inner wall of the nanopore (to account for the PEG molecule), and the intensity is calculated inside the nanopore (details in the Methods section). With a unitary dipolar emission, the emission is expected to decrease as the size of the pore is increased, since the emission rate is proportional to the inverse of the lifetime.<sup>20</sup> This is indeed what the simulations in Fig. 5(b) show. Furthermore, the near-field simulations depict the abrupt change in the slope between 170 and 250 nm, in the ATTO 590 graph. In the insets in Fig. 5(b) we show the e.m. near-field generated by the dipole excitation, for each of the four families. In the far-field intensity simulations the same trend holds: the intensity is higher for the smallest nanopores (Fig. 5d).

To estimate the mean Purcell Factor (or enhancement of the spontaneous decay rate,  $\Gamma/\Gamma_0$ ) induced by our decorated nanopores, we have experimentally measured the lifetime of the HS-PEG-NH-OC-ATTO dyes dropped on the gold-covered membrane, for comparison. The dyes were placed on the same membrane of the plasmonic structures, but far from their influence. Table 2 summarizes these lifetime measurements, and the calculated Purcell factors for all the families of nanopores decorated with the two dyes (one at the time). The lifetime on the golden membrane is close to 3.5 ns for both the dyes. From the comparison between these lifetimes and the previously reported nanopore lifetimes, we could calculate the Purcell factors relative to our nanopores to be comprised between 1 and 6, in accordance with those measured for similar structures.<sup>21</sup>

Dye	Lifetime (ns)	$\Gamma/\Gamma_0$ for A	$\Gamma/\Gamma_0$ for B	$\Gamma/\Gamma_0$ for C	$\Gamma/\Gamma_0$ for D
ATTO 520	$3.5 \pm 0.2$	$3.2 \pm 0.6$	$2.5 \pm 0.4$	$1.9 \pm 0.2$	$1.6 \pm 0.2$
ATTO 590	$3.6 \pm 0.1$	$6 \pm 1$	$5 \pm 3$	$1.5 \pm 0.2$	$1.3 \pm 0.1$

**Table 2.** Lifetime measurements of ATTO dyes dried off on the flat part of the membrane, and calculated Purcell factors for the four families of nanostructures.

The next step has been to characterize the FRET configuration. Through our selective functionalization protocol we have attached both ATTO dyes inside the nanopores, at the tip of our 3D antennas. With respect to the single dye experiments we halved the concentrations of the single dyes. It should be noticed that the FRET effects we measured are mean effects, since we couldn't control the distance between the D/A pairs. Fig. 6(a) shows the lifetime measured for the ATTO 520 dyes both in single and FRET configuration. Fig. 6(b) represents the FRET efficiency for the ATTO 520 dye on the four different families of nanopores, calculated from the data in Fig. 6(a). The efficiency is calculated as  $\eta_{FRET} = 1 - \tau_{DA}/\tau_D$  (see Methods). We can take different informations from these two graphs. First, in Fig. 6 (a) we see the trademark effect of FRET: the lifetime of the donor is shortened by the presence of the acceptor.

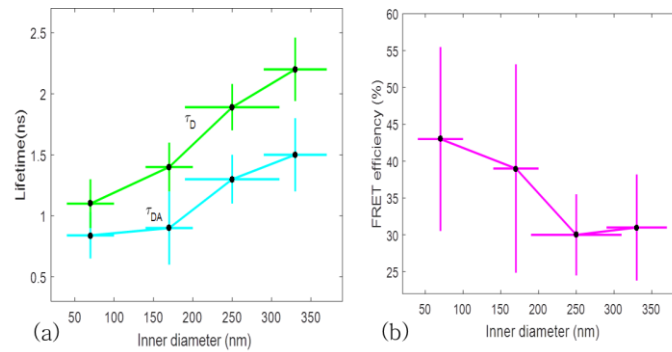
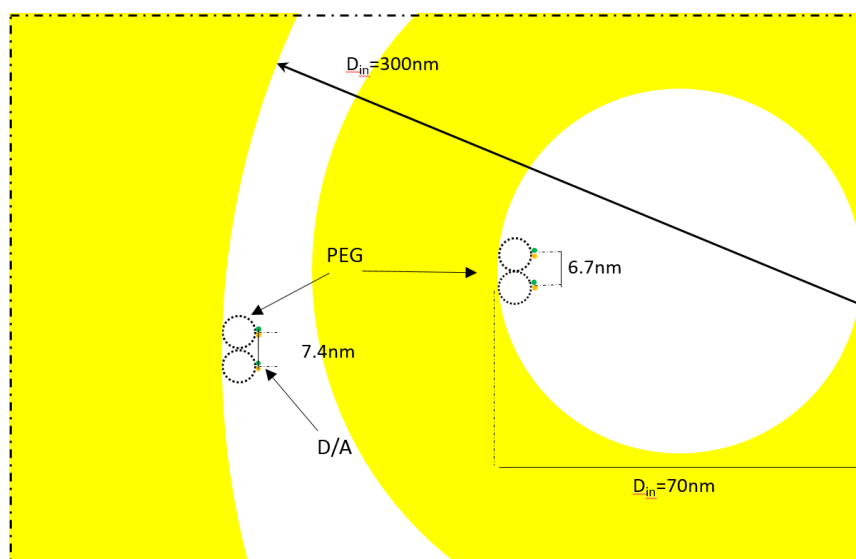


Fig. 6. (a) Lifetime measurements of site-selective functionalized plasmonic nanopores with single ATTO 520 and with ATTO 520 and ATTO 590 altogether. Each data point is the result of the measurement of two arrays of 49 nanopores (see Methods). The fluorescence from the ATTO 520 dyes has been measured in the 553-577 nm spectral band. (b) Average FRET efficiency for the ATTO520-ATTO590 FRET pair. From Zambrana-Puyalto X. et al., submitted 2018.<sup>16</sup>

Then, the graph in Fig. 6 (b) shows that the FRET efficiency is practically constant for the larger nanopores (30% and 31%), but it increases as the size of the nanopore shrinks. Even though we couldn't control the distance between the dyes, and that distance isn't constant, the efficiency values we calculated are similar to those obtained within other groups that tested similar structures.<sup>22</sup> The



dependence of efficiency on the size is quite intuitive. We can assume the dyes to be attached onto the wall of the nanopore with a constant density: there is the same number of dyes on each infinitesimal area of the nanopore. For the large nanopores, the FRET efficiency derives from the interaction between the dyes of this infinitesimal area: the dyes interact with their first neighbours, only, since the dyes in the other infinitesimal areas are more distant than the typical 1-20 nm FRET range. If the curvature of the inner walls is higher, the situation is different. The dyes from each infinitesimal area can interact with the neighbouring areas, increasing the FRET efficiency. This can be visualized in the sketch in Fig. 7. In the depicted toy model, the average distance between the FRET pair results reduced from 7.4 to 6.7 nm because of the increased curvature of the inner wall. This average distance values are surprisingly quite consistent with our experimental FRET radii, which are respectively  $7.5 \pm 0.9$  nm and  $6.8 \pm 0.8$  nm for the largest and smallest nanopores (see Methods). Our functionalization method seems to enable us to retrieve the curvature of the nanopore via lifetime measurements.



**Figure 7.** Sketch of the curvature influence on the FRET efficiency. The structure in the centre of the picture represents a nanopore with an inner diameter of  $D_{in}=70$  nm. The outer yellow represents a nanopore with an inner diameter of  $D_{in}=300$  nm. The PEG molecules are displayed as dashed circles of 6nm. The ATTO dyes are drawn as coloured dots at the end of the PEG molecules. A line orthogonal to the inner wall surface indicates the position of the dyes on the PEG molecule. From Zambrana-Puyalto X. et al., submitted 2018. <sup>16</sup>

### 3.3 Conclusions

In summary, in this chapter we have presented a site-selective functionalization technique to decorate metallic nanopores and we have characterized their spectroscopic properties. By slightly



modifying an already known fabrication protocol for 3D hollow nanoantennas, we were able to obtain isolated plasmonic rings. The robust fabrication technique enabled us to control the dimension of inner channel of the nanopore. The modulation of the dimension of the nanopores allowed us to both tailor their field confinement and their Purcell Factor in the visible spectral range. To investigate how the different dimensions of the nanopores influence the fluorescence emission, and thanks to the isolated-rings configuration, we anchored thiol-conjugated dyes on the plasmonic ring, thus forming a functional nanopore. To do that, we have modified the NHS-activated ATTO 520 and ATTO 590 dyes with a thiolate PEG. We have attached the HS-PEG-NH-OC-ATTO dyes to the plasmonic ring using a concentration gradient in between the two sides of the sample. We have functionalized the structures for four different nanopore sizes. We have observed that the emission efficiency of the plasmonic nanostructures increases as the inner diameter of the nanopore shrinks. This trend holds for both the single dye configurations and for the FRET pairs. In the case of FRET pairs, we observed that FRET efficiency increases for small sizes, whereas it reaches a plateau at the large sizes. The novel approach we presented, where plasmonic nanopores are used to enhance the fluorescence energy transfer, could open the way toward alternative detection methods in biosensing and sequencing. Acceptor dyes could be placed, for example, with our functionalization scheme, on a plasmonic ring on top of a nanochannel that connects two chambers. Donor labelled analytes could then be translocated through the nanochannel, and detected through the FRET interaction between donor and acceptor. In the case of DNA sequencing, a different donor dye could be attached to each of the 4 nucleotides, to distinguish between them upon their translocation through the pore. More sophisticated designs, with both donors and acceptors placed on the ring, would be necessary for label free sequencing. Despite the higher reading velocity of optical signals with respect to the electrical ones, DNA translocation speed remains an issue in sequencing applications, even in optical reading setups. In this respect, our plasmonic nanopores could be exploited even as plasmonic traps for the translocating analytes. The possibility of parallel readout represent, then, like in other optical sensing methods, a major advantage for our arrays of nanopores, with respect to electric signal based sensing schemes. In the direction of the mentioned new possible applications, the spectroscopic findings reported for our nanopores, which have been also supported by numerical simulations, may open new pathways to engineer the energy transfer in plasmonic nanopores.

## 3.4 Methods

### 3.4.1 Optical set-up

The experiments are performed on an inverted microscope with a long distance water-immersion microscope objective with NA=1.1. The light beam, which enters the microscope through its rear

port, is obtained with a fibred supercontinuum laser with a central wavelength of  $\lambda=532$  nm. The spectral bandwidth of the laser is  $\pm 5$  nm, the repetition rate is 78 MHz and the pulse width is approximately 65 ps. The power of the laser before entering the rear port of the microscope is 0.35  $\mu$ W. The samples that we use for the experiment are held on a sample holder, which is attached to a micro and a nanopositioner. The nanopositioner is used to centre the nanopore with respect to the incident beam. We consider that the nanopore is centred with respect to the beam when the fluorescence intensity is maximum. The nanopositioner is also used to place the sample at the z plane where the fluorescence counts are maximized. The detection of the fluorescence is done in reflection. The fluorescence is separated from the backscattering of the sample by means of three filters. Firstly, a notch dichroic filter at 532 nm and a longpass filter at 550 nm remove most of the backscattering. Then, a dichroic filter at 594 nm splits the fluorescence in two paths. The fluorescence on the path for wavelengths below 594 nm mostly belongs to the ATTO520, while the fluorescence for wavelengths longer than 594 nm is mostly due to the emission of ATTO590. A different third filter is added on each path. A bandpass filter at 565/24 nm (618/50 nm) is added on the path of detection of ATTO520 (ATTO590). An avalanche photodiode (APDs) is set up on each path to detect the fluorescence. The signal of the APDs is recorded with a time-correlated single photon counting module.

### 3.4.2 Lifetime measurements

The APDs, as well as the laser are connected to a time-correlated single-photon counting module (Swabian Instruments) in time-resolved mode. Making use of a home-built code, we build a histogram of 300 bins, each of them having a temporal width of 30 ps. A time delay of 6.56 ns is applied to the laser channel, so that the histogram is monotonously decreasing. The histogram measurement is carried out for 25 s, and it is repeated four times, yielding four histograms. A biexponential function of the kind  $Ae^{-t/\tau_a} + Be^{-t/\tau_b}$  is used to fit the decay curve for each histogram. Typically, the  $Ae^{-t/\tau_a}$  exponential contains information about the backscattering (or impulse response function), whereas  $Be^{-t/\tau_b}$  contains information about the fluorescence. This is easily observed, as the fluorescence signal tends to decrease over time due to the photobleaching of dyes which are illuminated for long periods close to a metallic surface. This photobleaching effect is usually captured in the fit by a decrease of the coefficient  $B$ . Then, measuring four histograms allows us to see if the lifetime measurement is stable over time, or not. We obtain the lifetime of a particular nanopore by doing a weighted arithmetic mean of the four lifetimes, the weights being  $B/A$ . The same measurement is carried out for each of the nanopores of the array (49 in total), and it is repeated for a second array. Then, the lifetime of the array is given as the average of all the significant lifetimes of the two arrays. The lifetime measurements that are not considered significant

are due to the fact that their value are more than  $2\sigma$  away from the average. The error of the measurement is obtained as the standard deviation associated to the average with the significant points.

### 3.4.3 FRET measurements

The FRET efficiency of the antennas is computed as  $\eta_{FRET} = 1 - \tau_{DA}/\tau_D$ , with  $\tau_D$  being the lifetime of the donor by itself and  $\tau_{DA}$  the lifetime of the donor when it is in the neighbourhood of an acceptor. Due to the fact that we cannot control the distances in between the donor and the acceptor, our experiments yield mean measurements of the FRET efficiency. The concentration of the donor has been maintained for both experiments, *i.e.* single donor and FRET pair. A control check with acceptor sensitization has not been performed because of our lack of control of the number of molecules and the decreasing fluorescence signal due to photobleaching. The error of  $\eta_{FRET}$  is computed doing a standard analysis of the statistical propagation of the uncertainty:

$$s_f = \sqrt{\sum_i \left(\frac{\partial f}{\partial x_i}\right)^2 s_{x_i}^2}.$$

The D/A mean distance is obtained using the expression  $R = R_0 \left(\frac{\tau_{DA}}{\tau_D - \tau_{DA}}\right)^{1/6}$ , where  $R_0 = 6.5$  nm is the Förster distance of the two ATTO dyes used in the experiment.<sup>23</sup>

### 3.4.4 Chemical modification of ATTO dyes

HS-PEG2000-NH<sub>2</sub> [mercapto poly(ethylene glycol) amine] (2,27 mg, 1,135  $\mu$ mol) were solubilised in 1 mL of MES 10 mM pH 8 (1,14 mM). From this stock solution, aliquots of 100  $\mu$ M of HS-PEG2000-NH<sub>2</sub> were prepared using the same buffer, MES 10 mM pH 8.

100  $\mu$ L of the HS-PEG2000-NH<sub>2</sub> aliquot were added to a solution of ATTO590-NHS ester (100  $\mu$ M) in MES 10 mM pH 8. The mixture was stirred at room temperature, at dark, overnight. The same procedure was followed to label HS-PEG2000-NH<sub>2</sub> with ATTO520-NHS ester. Even in such a case, the two reagents were used in the stoichiometric molar ratio of 10:1, respectively for the dye and PEG. The excess of dye was then removed by 24 hours of dialysis (cut-off membrane: 1 kDa). Once purified, the labelled PEG was lyophilised overnight (Lio5P, Kambic). The amount of dye effectively linked to PEG was quantified by measuring the absorbance in water of the labelled PEG and by means of the specific molar attenuation coefficient and Beer-Lambert law. The so prepared HS-PEG-NH-OC-ATTO590 and HS-PEG-NH-OC-ATTO520 were stored at  $-20^\circ\text{C}$  in aqueous solution and diluted at the desired concentration in EtOH prior surface functionalisation experiments.

Materials: ATTO520 NHS ester, BioReagent, suitable for fluorescence,  $\geq 80.0\%$  (coupling to amines), ATTO590 NHS ester, BioReagent, suitable for fluorescence,  $\geq 60\%$  (coupling to amines),

HS-PEG2000-NH<sub>2</sub> HCl Salt (average Mn 2,000) and 4-Morpholineethanesulfonic acid (MES) hydrate, ≥99.5%, were purchased from Sigma Aldrich. MES 10 mM pH 8 was prepared as followed: a stock solution of 100 mM MES was prepared solubilising MES hydrate (9,76 g, 50 mmol) in of DI water (500 mL); 10 mL of this solution were diluted with 90 mL of DI water reaching 10 mM as final concentration; the pH was adjusted to pH 8 adding 0,1 M NaOH dropwise. Spectrum™ Spectra/Por® 6 Standard RC Pre-wetted Dialysis Tubing MWCP 1 kD were purchased from Fisher.

### 3.4.5 Electromagnetic Simulations

Numerical simulations based on the Finite-Element Method implemented in the RF Module of Comsol Multiphysics® were carried out to investigate the electromagnetic response of an isolated nanopore. The dimensions of the simulated structures were set according to the average sizes obtained from SEM measurements. A dielectric constant  $n = 1.33$  was used for water, and  $n = 1.5$  was set for the glass substrate. The refractive index of Au was taken from Rakic.<sup>24</sup> The model computes the electromagnetic field in each point of the simulation region, enabling the extraction of the quantities plotted along the manuscript. The unit cell was set to be 1500 nm wide in both x- and y-directions and 2000 nm along the z-direction, with perfect matching layers (200 nm thick) at the borders. A linearly polarized Gaussian beam is tightly focused down to a spot size of  $w_0 = 350$  nm. The beam impinges on the top side of the structure, namely where the nanopore is placed, from the water side. The field intensity enhancement is computed as the average of field intensity in the volume of the nanopore. We define the volume as  $\pi D_{in}^2 t / 4$ , with  $t = 30$  nm being the width of the deposited gold ring.

For the simulations with the dipoles, a dipole oscillating along the in-plane direction of the nanopore at either 565 nm or 618 nm was placed at 6 nm from the inner wall of the nanopore for all the four cases treated in the manuscript. In this case the dipole is the only field source within the simulation region. The field intensity enhancement is also computed across the whole volume of the pore.

## References

- 1 O. N. Assad, T. Gilboa, J. Spitzberg, M. Juhasz, E. Weinhold and A. Meller, *Adv. Mater.*, 2017, **29**, 1605442.
- 2 J. Larkin, R. Y. Henley, V. Jadhav, J. Korlach and M. Wanunu, *Nat. Nanotechnol.*, 2017, 1–8.
- 3 C. Chen, Y. Li, S. Kerman, P. Neutens, K. Willems, S. Cornelissen, L. Lagae, T. Stakenborg and P. Van Dorpe, *Nat. Commun.*, , DOI:10.1038/s41467-018-04118-7.
- 4 G. A. Chansin, R. Mulero, J. Hong, M. J. Kim, A. J. DeMello and J. B. Edel, *Nano Lett.* ,

DOI:10.1021/nl071855d.

- 5 D. Punj, P. Ghenuche, S. B. Moparthy, J. de Torres, V. Grigoriev, H. Rigneault and J. Wenger, *Wiley Interdiscip. Rev. Nanobiotechnology*, 2014, **6**, 268–282.
- 6 P. Ponzellini, X. Zambrana-Puyalto, N. Maccaferri, L. Lanzanò, F. De Angelis and D. Garoli, *Nanoscale*, 2018, 17362–17369.
- 7 L. Restrepo-Pérez, C. Joo and C. Dekker, *Nat. Nanotechnol.*, 2018, **13**, 786–796.
- 8 J. van Ginkel, M. Filius, M. Szczepaniak, P. Tulinski, A. S. Meyer and C. Joo, *Proc. Natl. Acad. Sci.*, 2018, 201707207.
- 9 P. Ghenuche, J. De Torres, S. B. Moparthy and V. Grigoriev, *Nano Lett.*, 2014, **14**, 4707–4714.
- 10 J. de Torres, M. Mivelle, S. B. Moparthy, H. Rigneault, N. F. Van Hulst, M. F. García-Parajó, E. Margeat and J. Wenger, *Nano Lett.*, 2016, acs.nanolett.6b02470.
- 11 M. Oliverio, S. Perotto, G. C. Messina, L. Lovato and F. De Angelis, *ACS Appl. Mater. Interfaces*, , DOI:10.1021/acsami.7b01583.
- 12 A. Ananth, M. Genua, N. Aissaoui, L. Díaz, N. B. Eisele, S. Frey, C. Dekker, R. P. Richter and D. Görlich, *Small*, , DOI:10.1002/sml.201703357.
- 13 M. Pla-Roca, L. Isa, K. Kumar and E. Reimhult, *ACS Appl. Mater. Interfaces*, , DOI:10.1021/acsami.5b00138.
- 14 M. P. Jonsson, A. B. Dahlin, L. Feuz, S. Petronis and F. Höök, *Anal. Chem.*, , DOI:10.1021/ac902925e.
- 15 F. De Angelis, M. Malerba, M. Patrini, E. Miele, G. Das, A. Toma, R. P. Zaccaria and E. Di Fabrizio, *Nano Lett.*, 2013, **13**, 3553–3558.
- 16 X. Zambrana-Puyalto, N. Maccaferri, P. Ponzellini, G. Giovannini, F. De Angelis and D. Garoli, *Site-selective functionalization of plasmonic nanopores for enhanced fluorescence and Förster Resonance Energy Transfer*, .
- 17 J. Aizpurua, P. Hanarp, D. S. Sutherland, M. Käll, G. W. Bryant and F. J. García de Abajo, *Phys. Rev. Lett.*, 2003, **90**, 4.
- 18 D. Garoli, D. Mosconi, E. Miele, N. Maccaferri, M. Ardini, G. Giovannini, M. Dipalo and F. De Angelis, 2018, 17105–17111.
- 19 M. Zhengyu, N. L. B. David, M. L. Sharon, A. S. Kim, L. K. Michael, E. D. Dennis and H. F. Terri, *PLoS One*, 2014, **9**, 1–10.
- 20 L. Novotny and B. Hecht, *Principles of Nano-Optics*, 2006.
- 21 J. De Torres, P. Ghenuche, S. B. Moparthy, V. Grigoriev and J. Wenger, *ChemPhysChem*, 2015, **16**, 782–788.
- 22 D. J. Roth, M. Nasir, P. Ginzburg, P. Wang, A. Le Marois, K. Suhling, D. Richards and A. V Zayats, *ACS Photonics*, 2018, acsphotronics.8b01083.
- 23 I. Medintz and N. Hildebrandt, *FRET - Förster Resonance Energy Transfer*, 2013.
- 24 A. D. Rakić, A. B. Djurišić, J. M. Elazar and M. L. Majewski, *Appl. Opt.*, 1998, **37**, 5271.



## 4. Controlled deposition of MoS<sub>2</sub> flakes on metallic nanopores by means of an electrophoretic process

### 4.1 Introduction

In the third chapter we have shown how our 3D hollow antennas can allow for a simple, fast and effective protocol for site-selective dye functionalization of plasmonic nanopores. In such a way we were able to exploit the plasmonic hotspot at the top of our antennas to enhance dye fluorescence and FRET between the attached dyes. In the fabrication presented here, we have used the same 3D hollow antennas invented within our group,<sup>1</sup> as well as more traditional flat plasmonic nanopores, to develop an easy and robust protocol for integrating MoS<sub>2</sub> 2D flakes onto plasmonic nanopores.

In the last decade, intensive research efforts have been devoted to the investigation of two dimensional (2D) materials, such as graphene and various transition metal chalcogenides (TMDCs)<sup>2-5</sup> Molybdenum disulfide (MoS<sub>2</sub>) is a typical representative of the TMDCs material family, and consists of S-Mo-S layers bonded by a Van Der Waals interaction. MoS<sub>2</sub> offers a powerful platform for applications in nanophotonics and optoelectronics due to its remarkable optical properties. In fact, MoS<sub>2</sub> behaves like a semiconductor with direct band gap electronic structure, notable flexibility, and tunable optical emission.<sup>6,7</sup> Owing to its atomically thin layer, monolayer MoS<sub>2</sub> can be easily integrated with other low-dimensional materials such as quantum dots,<sup>7</sup> nanowires,<sup>8,9</sup> and other 2D materials<sup>10</sup> to form hybrid nanostructures with intriguing electronic and optical properties.

Regarding MoS<sub>2</sub> optical properties, great efforts have been devoted to realize the active control of MoS<sub>2</sub> by utilizing photonic cavity modes and metallic surface plasmons, in order to enhance and modulate its quantum optical properties. The aim is generally to explore the potential physical phenomena of MoS<sub>2</sub>, especially on light-matter interaction, such as multiexciton PL, interlayer exciton coupling, strong coupling and valley polarization effect. However, hybrid plasmonic-2D systems have been proposed and can be engineered for sensing purposes too, for example for enhancing the fluorescent signal from molecules translocating through a 2D nanopore,<sup>11</sup> or for trapping molecules in correspondence with a graphene nanopore.<sup>12</sup> A plasmonic hotspot localized on a MoS<sub>2</sub> layer could then be helpful for example in experiments where MoS<sub>2</sub> is used as a fluorescence quencher, to detect nanoparticles<sup>13</sup> or biomolecules<sup>14</sup> from fluorescence signals.

One of the main limitation of MoS<sub>2</sub> application in photonics and plasmonics is related to the challenging alignment between nanostructures and the 2D material. New approaches for easy and controlled integration of 2D materials with metallic or semiconductor nanostructures can hence

represent a significant help in the cited fields of research, and in sensing applications in particular. It has been recently proposed and demonstrated, within our group, the possibility to control the deposition of single layer MoS<sub>2</sub> flakes on metallic nanostructures by means of chemical conjugation.<sup>15</sup> The novel approach we present here is based on an electrophoretic deposition where the substrate does not act as an electrode. It can be in principle applied to any substrate endowed with nanoapertures to be decorated with MoS<sub>2</sub> flakes in the form of single or few layers, since it allows high yield controlled deposition on both flat and 3D nanopores like our 3D hollow antennas.

## 4.2 Results and Discussion

The deposition process is illustrated in Fig. 1 (Top Panel). The MoS<sub>2</sub> flakes preparation, based on chemical exfoliation,<sup>16,17</sup> is described in the methods section; Fig. 1,2 show examples of the ordered deposition of single flakes on top of metallic nanoholes and 3D gold nanostructures. The method used for the deposition is based on the net mean charge of the MoS<sub>2</sub> in solution. As shown in Table1, MoS<sub>2</sub> flakes have a negative surface charge ( $-39,57 \text{ mV} \pm 0,38 \text{ mV}$ ) in deionized water, which is even suggested by their zeta potential ( $\zeta$ ) value measured by Dynamic Light Scattering (DLS).  $\zeta$  is also known as electrokinetic potential, which is the potential at the surface-fluid interface of a colloid moving under electric field. Once the charged MoS<sub>2</sub> flakes are dispersed in water, ions of the opposite charge are absorbed at the surface, thus forming a layer of closely adhered ions (the Stern layer). At increasing distances from the surface, the Stern layer transforms into a diffuse and dynamic layer of a mixture of ions. Together, the Stern and the diffuse layer constitute the electric double layer (EDL). The EDL determines the mobility of the flakes in suspension under electric field, which corresponds to the  $\zeta$  measured by DLS.<sup>18</sup> For this reason, the net surface charge of the flakes is almost neutral in organic solvents like ethanol ( $-3,66 \pm 0,28 \text{ mV}$ ) where the EDL is different. This dramatically influences the electrophoretic mobility of the MoS<sub>2</sub> flakes which is  $-3,10 \pm 0,03 \text{ } \mu\text{mcm/Vs}$  in water and  $-0,54 \pm 0,04 \text{ } \mu\text{mcm/Vs}$  in ethanol (Table1).

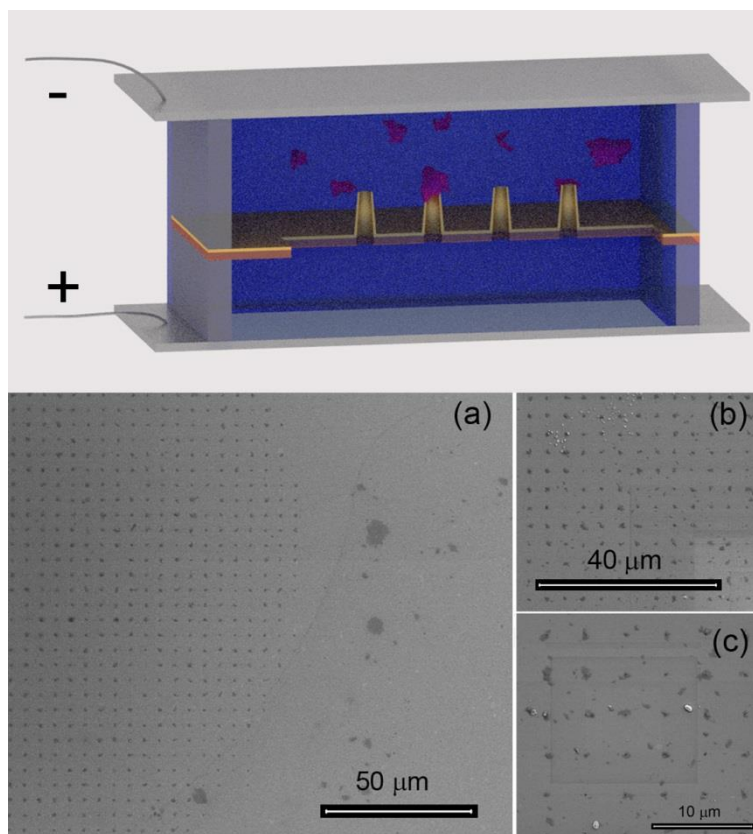
	DI water	Ethanol
Zeta potential (mV)	$-39,57 \pm 0,38$	$-3,66 \pm 0,28$
Electrophoretic Mobility ( $\mu\text{mcm/Vs}$ )	$3,10 \pm 0,03$	$-0,54 \pm 0,04$

Table 3. Zeta potential and electrophoretic mobility of the MoS<sub>2</sub> flakes measured by DLS in water and ethanol. Values are reported as average number (n=3)  $\pm$  SD.



The charged surface of the flakes suggests the possibility to deposit MoS<sub>2</sub> by applying a voltage, to realize an electrophoretic deposition (Fig. 1). The electrophoretic deposition method has been already reported for MoS<sub>2</sub> nanosheets for several applications.<sup>19,20</sup> Here, with respect to the previously reported protocols, we don't use the substrate on which the flakes are deposited as an electrode. On the contrary, in order to obtain a controlled deposition only over our nanostructures, we place the substrate inside a fluidic chamber where two Pt electrodes are present, one at each side of the substrate. In particular, the nanoholes on the substrate allow for ionic flow through them but are an obstacle for the MoS<sub>2</sub> flakes: MoS<sub>2</sub> flakes are forced to stop and deposit on the nanopores. The deposition protocol is illustrated in Fig. 1-Top Panel:<sup>21</sup> 1) we prepared the plasmonic holes on a Si<sub>3</sub>N<sub>4</sub> membrane (see methods); 2) we cleaned the sample in oxygen plasma for 1 minute; 3) we placed the sample at the ground state inside the microfluidic chamber. The chamber was endowed with two Pt electrodes; 4) we dispersed the MoS<sub>2</sub> flakes in H<sub>2</sub>O and injected them in the Cis side of the microfluidic chamber. The Trans side was filled with MilliQ H<sub>2</sub>O only; 5) we applied a suitable voltage for a time optimized to allow the electrophoretic deposition; and 6) we opened the chamber and rinsed the sample in EtOH: the controlled deposition was achieved. This method could be used in principle on every nanostructure endowed with a nanohole; anyway, we observed that the process had few critical aspects, within our configuration. First, we studied the deposition method on large rectangular matrices of flat metallic nanoholes. In this design, the substrate is a Si<sub>3</sub>N<sub>4</sub> membrane covered with a 100 nm thick gold layer where holes with a 100 nm diameter have been drilled using FIB lithography. As shown in Fig. 1, the electrophoretic deposition, carried out with an applied voltage of 2V over 5 minutes, leads to a well-distributed array of MoS<sub>2</sub> flakes covering the nanoholes. However, it seems that the holes on the edges of the square of the array did not receive the right ion flow and were not deposited. This may be due to the configuration of the electric field inside our chamber and could probably be overcome by increasing the size of the system. We also compared this deposition process with a simple drop cast (20 μL of MoS<sub>2</sub> in H<sub>2</sub>O let dry and rinsed in EtOH) on the same structure. As expected, in the latter case the substrate appears to be randomly coated, although a large number of holes are still coated. Repeating the electrophoretic deposition process on several identical samples shows poor reproducibility in terms of quality of the deposited flakes. In fact, even when testing different durations of the applied voltage, it seems difficult to control the number of layers covering the different nanopores. As will be shown below, it is possible to obtain more than 80% of the metal holes covered with MoS<sub>2</sub> but the number of holes decorated with a single-layer scale is low. The measurement of the number of deposited layers is reported below, as obtained by means of Raman spectroscopy, which allows to discriminate among single- or few-layer.<sup>22</sup> We investigated the possible reasons for the observed low reproducibility.

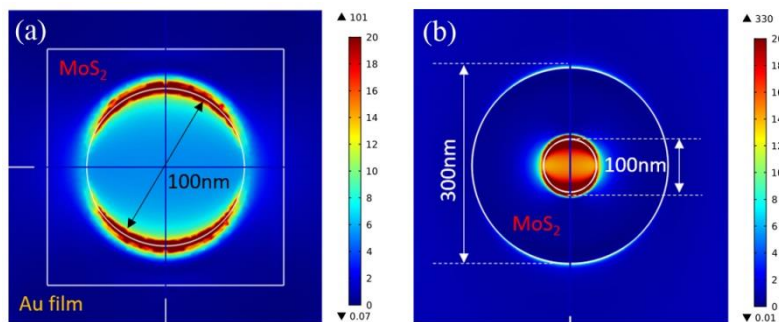
Firstly we compared the  $\zeta$  values for freshly prepared flakes with those of flakes that had been stored in water for several weeks and we further measured the surface charge of different MoS<sub>2</sub> samples. The results confirmed how the mean net charge was always negative, and almost constant at about -38 mV. Secondly, since MoS<sub>2</sub> is known to act as catalyst in reduction reactions,<sup>23</sup> we decided to investigate if this could potentially influence their surface charge. By treating MoS<sub>2</sub> with a solution of a strong oxidant (KMnO<sub>4</sub>) we noticed that, even though the reduction occurs (as confirmed by the change in color of the samples, from purple to brownish) the surface charge turns only slightly more positive: from -38 to -27 mV. This would only marginally change electrophoretic mobility, so that the catalytic activity of MoS<sub>2</sub> flakes cannot be associated with the low deposition reproducibility.



**Figure 1.** Top Panel: Illustration of the electrophoretic process; (a-c) SEM micrographs of gold nanohole arrays decorated with MoS<sub>2</sub> flakes by means of electrophoretic deposition. From Mosconi et al., submitted 2018.<sup>21</sup>

Once demonstrated the proof-of-concept deposition, we moved to test its applicability to 3D structures (Fig. 3(a-d)). 3D plasmonic structures comprising a nanochannel/nanohole can be fabricated with several different designs and materials, as recently reported.<sup>24,25</sup> The main feature of these particular nanostructures is that they can confine and enhance the e.m. field in a small gap at

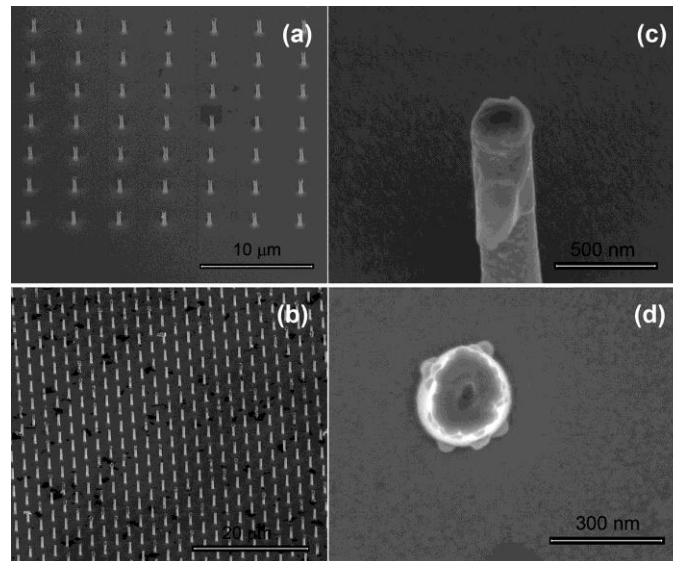
the top of the structure. With respect to a typical nanohole on a flat metallic layer, the field enhancement can be significantly higher, while the integrated nanochannel can be exploited as a nanofluidic element. To illustrate this enhancement we performed computer simulations (see Methods for details) for the two structures investigated: the nanoholes and the 3D antennas. Fig. 2 illustrates the field confinement / enhancement achievable in the two configurations. In the case of the MoS<sub>2</sub> flakes deposited on top of the 3D antenna (Fig. 2(b)) the e.m. field is more confined and reaches higher values, compared to a flat nanohole (Fig. 2(a)).



**Figure 2.** Finite Element Method (FEM) simulations of the investigated structures on which MoS<sub>2</sub> has been deposited. (a) Top view of e.m. field intensity ( $|E|^2$ ) in the case of nanohole on metallic (Au) film covered with a MoS<sub>2</sub> layer; (b) Top view of  $|E|^2$  in the case of 3D Au antenna covered with a MoS<sub>2</sub> layer. In both the case the MoS<sub>2</sub> layer covers a 100 nm large hole. From Mosconi et al., submitted 2018.<sup>21</sup>

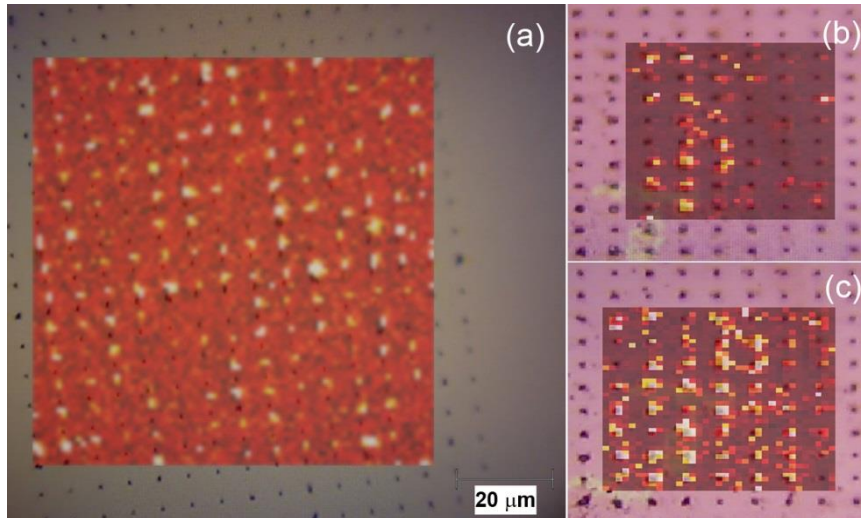
Fig. 3 shows few examples of Mo<sub>2</sub> flakes electrophoretic deposition on these substrates. As reported above, the 3D vertical antennas can be fabricated with different aspect-ratios, ranging from few hundreds of nm up to few  $\mu\text{m}$  in height. With respect to the flat metallic holes, the electrophoretic force applied through the higher antennas is not as efficient for the deposition. We expected the higher antennas to introduce a much higher resistivity in the ion flow and, in fact, we couldn't get a reproducible deposition. Decreasing the height to 1  $\mu\text{m}$  and increasing the diameter of the inner channel (see methods for details) we could obtain the ordered deposition. However, the required voltage is here quite higher with respect to the flat case, and to obtain a high rate of deposited antennas we needed to raise the voltage up to 15 V. Fig. 2(a,b) illustrate this evidence on similar samples. On the first one we applied a voltage of 10 V over 10 minutes, in the second the voltage was increased to 15 V, allowing for a more efficient deposition. Unfortunately, as a drawback, many flakes deposited also on the outer walls of the 3D antennas. In all the cases, anyway the procedure resulted in a partially covering layer that crinkles around the metal in many different ways, ranging from small flakes covering only the top hole to large flakes wrapping the

3D body of the structure. To verify the effectiveness of the MoS<sub>2</sub> deposition and to quantify the number of layers deposited over the different pores, we performed Raman spectroscopy on our samples at an excitation wavelength of 532 nm. The measurements were performed with a Rainshaw InVia Microscope Raman system with a 50 × 0.95 NA objective, collecting the signal with a spectral resolution of 2.5 cm<sup>-1</sup> and with an integration time of 1s. We calibrated the system with the intensity of the standard peak at 520 cm<sup>-1</sup> from a silicon substrate.



**Figure 3.** SEM micrographs of 3D antennas decorated with MoS<sub>2</sub> flakes by means of electrophoretic deposition. (a) 10 V applied voltage, 10 minutes; (b) 15 V applied voltage, 10 minutes; (c) and (d) details of deposited flakes. From Mosconi et al., submitted 2018.<sup>21</sup>

The results of our measurements are reported in Fig. 4. Fig. 4(a) shows the Raman map referred to a large arrays of flat metallic nanopores. Fig. 4(b,c) refer to 3D antennas. We used Raman shifts (at the excitation wavelength of 532 nm) between 400 and 410 cm<sup>-1</sup> (in correspondence of A<sub>1g</sub> Raman mode) to evaluate the amount of MoS<sub>2</sub> over the map. These figures indicate a significant difference among the samples. In the case of the flat metallic nanopores, where the deposition results efficient also at low voltages, the signal comes from the positions of the nanostructures only. This clearly demonstrates that our deposition procedure covers the desired elements.

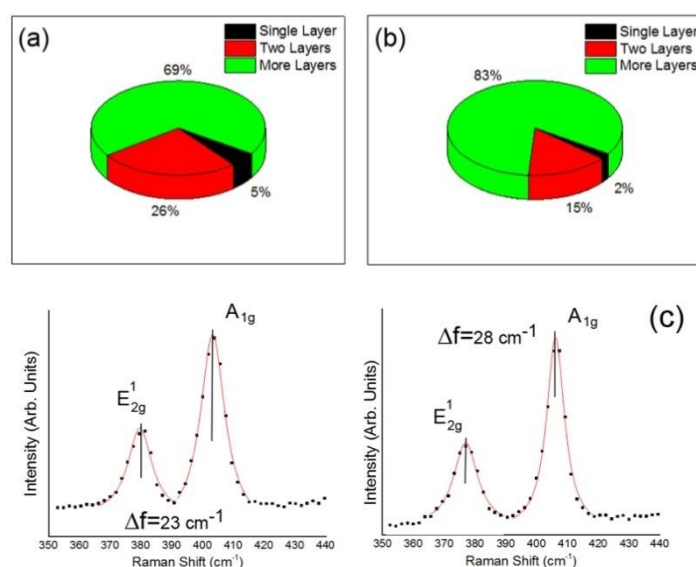


**Figure 4.** Raman maps reporting shifts between 400 and 410  $\text{cm}^{-1}$  (in correspondence of  $A_{1g}$  Raman mode). (a) Map over 190 nanoholes; (b) map over 3D antennas deposited at 10V for 10 minutes; (c) map over 3D antennas deposited at 15V for 10 minutes. From Mosconi D. et al., submitted 2018.<sup>21</sup>

Over 80 % of the holes are decorated with  $\text{MoS}_2$  flakes. The maps measured for the 3D antennas, instead, show what we observed by means of the SEM microscope. At 10 V only half of the antennas are decorated. Raising the voltage up to 15 V it's possible to deposit  $\text{MoS}_2$  flakes over almost all the structures, but even other parts of the substrate result covered.

As mentioned, we used Raman spectrum analysis to evaluate the number of  $\text{MoS}_2$  layers deposited on the samples. In Figure 5(a,b) the statistical analysis about the different measured points is reported for the flat nanoholes and for the 3D nanoantennas sample. The measured points have been fitted with Lorentzian functions (Fig. 5c). The in-plane ( $E_{2g}^1$  at  $\sim 380 \text{ cm}^{-1}$ ) and out-of-plane ( $A_{1g}$  at  $\sim 404 \text{ cm}^{-1}$ ) Raman modes were always well visible and hence used in the analysis. The difference between the  $E_{2g}^1$  and  $A_{1g}$  modes ( $\Delta f$ ) is known to steadily increase with the number of layers; hence, this parameter can be assumed as a reliable quantity for counting the number of  $\text{MoS}_2$  layers. We used  $\Delta f$  to quantify the fraction of single, double and multilayer flakes decorating the considered array. We consider “1 Layer” if  $\Delta f$  is equal to  $18 \text{ cm}^{-1}$ , “2 Layers” when it is  $22 \text{ cm}^{-1}$  and “more layers” when it is above  $23 \text{ cm}^{-1}$ . We concluded that for flat nanopores (Fig. 5a), a single layer deposition is rare (approximately 5 % of the pores), while most of the deposited flakes are found to be double layers (26%) or more than two layers (Fig. 5b). This is even accentuated for 3D nanoantennas where, because of the high voltage used in the deposition, single layer flakes are even more rare: the most of them resulted to be constituted of two or more layers. This can hopefully be improved by acting on the electrophoretic process parameters and on the exfoliation procedure, to obtain better-quality, single-layer flakes in solution. Indeed, here we chose a Li-intercalation procedure that, with respect to liquid-phase exfoliation, can provide stable suspensions without any surfactant (that may hamper both anchoring and plasmonic behavior) and with higher exfoliation

degree,<sup>23</sup> which, in our case, was maximized by doubling the Li dose. Unfortunately, MoS<sub>2</sub> tends to break up easily during the exfoliation, yielding a quite large size dispersion. Our deposition procedure proved to work with all the nanosheet sizes. Anyway we believe that by improving the synthetic procedure in such a way to obtain flakes with homogenous thickness and a controlled lateral dimension we would be able to further optimize the deposition and, consequently, to improve the performances of these hybrid nanostructures. Furthermore, by switching from chemical to electrochemical intercalation, the Li-exfoliation procedure may be scaled-up.<sup>26</sup> With this process it would be possible to prepare single-layer MoS<sub>2</sub> with higher throughput, which is a necessary condition for applying these systems at a large scale.



**Figure 5.** Statistical analyses based on Raman spectrum to evaluate the number of deposited MoS<sub>2</sub> layers. (a) Metallic nanoholes deposited at 2V; (b) 3D nanoantennas deposited at 15V; (c) examples of analyzed spectrum. From Mosconi D. et al., submitted 2018.<sup>21</sup>

### 4.3 Conclusions

In summary, we have presented in this chapter a method for preparing a hybrid plasmonic 2D material. The described fabrication allowed us to obtain large arrays of ordered structures by means of a low-cost procedure and without any complex lithographic processes. Besides MoS<sub>2</sub>, our scheme can be applied to many 2D materials whose surface net charge can be used to guide the electrophoretic process. With respect to previously reported hybrid plasmonic nanostructures, our scheme significantly reduces the fabrication procedure complexity, leading to a more robust approach for integrating 2D materials flakes within plasmonic nanopores. Importantly, our simulations show that the plasmonic field generated by the nanopores is well localized in proximity



of the 2D layer, making our structures ideal for investigating hybrid 2D-Material/Plasmonic systems.

Our approach could be useful even for realizing new hybrid devices for several applications, including sensing. As, they are, our MoS<sub>2</sub>-nanopores structures could be used to enhance the detection of freely diffusing analytes, for example by exploiting the fluorescence quenching property of MoS<sub>2</sub>. As for the case of our plasmonic ZMW, a hole could be drilled inside the MoS<sub>2</sub> layer to create a 2D plasmonic nanopore. In such a flow through configuration, several sensing approaches would be possible. The electric readout detection schemes could take advantage of the 2D pore optimal spatial resolution and at the same time of the enhanced e.m. field for a simultaneous electric-optical readout. The plasmonic hotspot could be then exploited for enhancing the fluorescence signal of a translocating molecule. Finally, plasmonic trapping could be of benefit, whatever the detection approach, to slow down the analyte translocation, especially for sequencing purposes.

## 4.4 Methods

### 4.4.1 Exfoliation of MoS<sub>2</sub>

In a glove-box (water < 1 ppm, O<sub>2</sub> < 10 ppm), we ground LiBH<sub>4</sub> (0.109 g, 5 mmol) and MoS<sub>2</sub> (0.320 g, 2 mmol) in a mortar and subsequently transferred them in a Schlenk-tube. Then we brought it outside of the glove-box and connected it to a Schlenk-line. Hence we heated the mixture at 330°C in a sand bath, for 4 days in nitrogen atmosphere. Then we brought the Schlenk-tube back inside the dry-box, where we ground it again with additional LiBH<sub>4</sub> (0.109 g, 5 mmol). We then heated the sample for 3 days at 330°C in nitrogen atmosphere.

Subsequently we added the intercalation product in a single shot in 270 ml of degassed water and we sonicated the resulting suspension for 1 h in order to facilitate the exfoliation.

To remove the produced LiOH, we equally divided the suspension into six centrifugation tubes (45 ml/tube) and centrifuged at 10000 rpm (23478g) for 20 min for three times, replacing the supernatant with clean solvent.

To select the flake size, we progressively centrifuged the suspension purified by LiOH at 8000 (15026g – 8K fraction), 6000 (8452g – 6K), 4000 (3757g – 4K), 3000 (2113g – 3K), 2000 (939g – 2K) and 1000 rpm (235g – 1K), each time collecting the top 2/3 of the supernatant and replacing it with ultrapure water.

#### 4.4.2 Fabrication of plasmonic nanostructures

For the fabrication of the nanopores, both in the 2D and 3D geometry, the substrate used was a  $\text{Si}_3\text{N}_4$  membrane (100 nm thick) prepared on a Silicon chip. We fabricated the 2D hole by means of FIB milling with a current of 80 pA. After the milling, we deposited a thin layer of gold, about 100 nm, on the top side of the membrane. The fabrication of 3D nanoholes array followed the same procedure as in the third chapter, except from the metal deposition part. In fact, after the development in acetone, we have sputter deposited about 40 nm of gold on our hollow antennas. For these experiment 3D antennas with inner diameter between 30 and 100 nm and final height between 1000 and 2000 nm have been prepared, using different FIB currents.

#### 4.4.3 FEM Simulation of $\text{MoS}_2$ flakes integrated over plasmonic nanostructures

We investigated the plasmonic properties of the structure by means of finite element method (FEM) simulations by using the RF Module in Comsol Multiphysics, taking into account the geometries that could be actually fabricated. We considered a hole of 100 nm diameter into  $\text{Si}_3\text{N}_4//\text{Au}$  100//50 nm membrane. Moreover, in the case of 3D antennas we considered a 1000 nm height antenna with inner and outer diameter of 100 and 300 nm respectively. A top single layer of  $\text{MoS}_2$  has been considered in both the cases.

Numerical simulations based on the Finite-Element Method implemented in the RF Module of Comsol Multiphysics® were carried out to investigate the electromagnetic response of isolated plasmonic nanohole and 3D antenna. The dimensions of the simulated structures were set taking into account the geometries that could actually be fabricated. We considered a hole of 100 nm diameter into  $\text{Si}_3\text{N}_4//\text{Au}$  100//50 nm membrane. Moreover, in the case of 3D antennas we considered a 1000 nm height antenna with inner and outer diameter of 100 and 300 nm respectively. A top single layer of  $\text{MoS}_2$  has been considered in both the cases. The model computes the electromagnetic field in each point of the simulation region, enabling the extraction of the quantities plotted in the graphs. The unit cell was set to be 400 nm wide in both x- and y-directions, with perfect matching layers (150 nm thick) at the borders.

## References

- 1 F. De Angelis, M. Malerba, M. Patrini, E. Miele, G. Das, A. Toma, R. P. Zaccaria and E. Di Fabrizio, *Nano Lett.*, 2013, **13**, 3553–3558.
- 2 A. K. Geim and K. S. Novoselov, *Nat. Mater.*, 2007, **6**, 183–191.
- 3 S. Agnoli and G. Granozzi, *Surf. Sci.*, 2013, **609**, 1–5.
- 4 R. Mas-Ballesté, C. Gómez-Navarro, J. Gómez-Herrero and F. Zamora, *Nanoscale*, 2011, **3**, 20–30.
- 5 M. Chhowalla, H. S. Shin, G. Eda, L.-J. Li, K. P. Loh and H. Zhang, *Nat. Chem.*, 2013, **5**, 263–275.



- 6 L. P. Zaino, D. A. Grismer, D. Han, G. M. Crouch and P. W. Bohn, *Faraday Discuss.*, 2015, **184**, 101–115.
- 7 F. Prins, A. J. Goodman and W. A. Tisdale, *Nano Lett.*, , DOI:10.1021/nl5019386.
- 8 K. M. Goodfellow, R. Beams, C. Chakraborty, L. Novotny and A. N. Vamivakas, *Optica*, , DOI:10.1364/OPTICA.1.000149.
- 9 H. S. Lee, M. S. Kim, Y. Jin, G. H. Han, Y. H. Lee and J. Kim, *Phys. Rev. Lett.*, , DOI:10.1103/PhysRevLett.115.226801.
- 10 A. K. Geim and I. V. Grigorieva, *Nature*, 2013.
- 11 S. Nam, I. Choi, C. Fu, K. Kim, S. Hong, Y. Choi, A. Zettl and L. P. Lee, *Nano Lett.*, 2014, **14**, 5584–5589.
- 12 B. Fotouhi, V. Ahmadi and M. Abasifard, *Sci. Iran. F*, , DOI:10.24200/sci.2018.20419.
- 13 K. Srinivasan, K. Subramanian, K. Murugan and K. Dinakaran, *Analyst*, 2016, **141**, 6344–6352.
- 14 C. Zhu, Z. Zeng, H. Li, F. Li, C. Fan and H. Zhang, *J. Am. Chem. Soc.*, 2013, **135**, 5998–6001.
- 15 D. Garoli, D. Mosconi, E. Miele, N. Maccaferri, M. Ardini, G. Giovannini, M. Dipalo, S. Agnoli and F. De Angelis, *Nanoscale*, , DOI:10.1039/c8nr05026k.
- 16 D. Voiry, M. Salehi, R. Silva, T. Fujita, M. Chen, T. Asefa, V. B. Shenoy, G. Eda and M. Chhowalla, *Nano Lett.*, , DOI:10.1021/nl403661s.
- 17 M. Acerce, D. Voiry and M. Chhowalla, *Nat. Nanotechnol.*, , DOI:10.1038/nnano.2015.40.
- 18 S. Bhattacharjee, *J. Control. Release*, 2016.
- 19 M. S. Nam, U. Patil, B. Park, H. B. Sim and S. C. Jun, *RSC Adv.*, , DOI:10.1039/c6ra16078f.
- 20 Y. Liu, L. Ren, Z. Zhang, X. Qi, H. Li and J. Zhong, *Sci. Rep.*, , DOI:10.1038/srep22516.
- 21 D. Mosconi, A. Jacassi, G. Giovannini, P. Ponzellini, N. Maccaferri, P. Vavassori, M. Dipalo, F. De Angelis, S. Agnoli and D. Garoli, *Controlled integration of MoS<sub>2</sub> flakes on nanopores by means of electrophoretic deposition*, .
- 22 C. Lee, H. Yan, L. E. Brus, T. F. Heinz, J. Hone and S. Ryu, *ACS Nano*, , DOI:10.1021/nn1003937.
- 23 L. Guardia, J. I. Paredes, J. M. Munuera, S. Villar-Rodil, M. Ayán-Varela, A. Martínez-Alonso and J. M. D. Tascón, *ACS Appl. Mater. Interfaces*, , DOI:10.1021/am506922q.
- 24 D. Garoli, P. Zilio, Y. Gorodetski, F. Tantussi and F. De Angelis, *Nano Lett.*, , DOI:10.1021/acs.nanolett.6b03359.
- 25 D. Garoli, E. Calandrini, A. Bozzola, M. Ortolani, S. Cattarin, S. Barison, A. Toma and F. De Angelis, *Nanoscale*, , DOI:10.1039/c6nr08231a.
- 26 Z. Zeng, Z. Yin, X. Huang, H. Li, Q. He, G. Lu, F. Boey and H. Zhang, *Angew. Chemie - Int. Ed.*, , DOI:10.1002/anie.201106004.